Vortices, skyrmions, and chirality waves in frustrated Mott insulators with a quenched periodic array of impurities

Satoru Hayami,[1] Shi-Zeng Lin,[2] Yoshitomo Kamiya,[3] and Cristian D. Batista[4,5]

[1]*Department of Physics, Hokkaido University, Sapporo 060-0810, Japan*

[2]*Theoretical Division, T-4 and CNLS, Los Alamos National Laboratory, Los Alamos, New Mexico 87545, USA*

[3]*Condensed Matter Theory Laboratory, RIKEN, Wako, Saitama 351-0198, Japan*

[4]*Department of Physics, University of Tennessee, Knoxville, Tennessee 37996, USA*

[5]*Quantum Condensed Matter Division and Shull-Wollan Center, Oak Ridge National Laboratory, Oak Ridge, Tennessee 37831, USA*

Finite-Q magnetic instabilities are rather common in frustrated magnets. When the magnetic susceptibility is maximized at multiple-Q vectors related through lattice symmetry operations, exotic magnetic orderings such as vortex and skyrmion crystals may follow. Here, we show that a periodic array of nonmagnetic impurities, which can be realized through charge density wave ordering, leads to a rich phase diagram featuring a plethora of chiral magnetic phases, especially when there is a simple relation between the reciprocal vectors of the impurity superlattice and the magnetic Q vectors. We also investigate the effect of changing the impurity concentration or disturbing the impurity array with small quenched randomness. Alternative realizations of impurity superlattices are briefly discussed.

I. INTRODUCTION

The emergence of nonzero bulk spin-scalar chirality, known as chiral order, has drawn considerable interest in condensed matter physics. Various consequences of a chiral order have been discussed in different fields ranging from superconductivity to Mott insulators [1–4]. An attractive area of research is generated by potential realizations of chiral liquid states, i.e., states that exhibit chiral order in absence of magnetic order [2,5–7]. Another attractive aspect of chiral states is their potential for inducing nontrivial topological phenomena, such as topological anomalous Hall effect for electrons coupled to a chiral spin state through the Berry phase mechanism [8–13]. The very large fictitious magnetic field produced by this mechanism (10^3–10^4 T) may bring major advances for spintronics applications [14]. It is then important to understand the physical mechanisms to stabilize the chiral order.

Noncoplanar magnetic orderings are accompanied by a nonzero local scalar chirality $\langle \chi_{jkl} \rangle = \langle \mathbf{S}_j \cdot (\mathbf{S}_k \times \mathbf{S}_l) \rangle \neq 0$, where j, k, and l are three neighboring lattice sites. Recent theoretical studies on frustrated Kondo lattice models have unveiled a general mechanism for stabilizing noncoplanar magnetic orderings in itinerant magnets comprising conduction electrons coupled to localized magnetic moments [13,15–20]. The mechanism relies on the generation of four- and higher-spin interaction terms, which appear upon expanding in the small Kondo interaction beyond the Ruderman-Kittel-Kasuya-Yosida (RKKY) level [17–19]. These multispin interactions are relatively weak in strongly coupled Mott insulators. In terms of a Hubbard model description with hopping amplitude t and onsite Coulomb potential U, four-spin interactions are of order $O(t^4/U^3)$, while two-spin interactions are $O(t^2/U)$. Consequently, chiral spin textures are less common in Mott insulators with isotropic exchange interactions. Indeed, these systems usually exhibit a conical spiral order with zero net scalar chirality even in an external magnetic field, otherwise either collinear or coplanar orderings. However, recent theoretical studies in both classical [21–25] and quantum [26–28]

frustrated spin systems have shown that the interplay between geometric frustration, thermal [21] or quantum fluctuations [26–28], magnetic anisotropy [22–25,29–31], and long-range (dipolar) interactions [32–34], can stabilize a plethora of multiple-Q spin textures in Mott insulators, some of which have net scalar spin chirality. In this context, it is worth mentioning a recent experimental confirmation of a triple-Q vortex crystal in the scandium thiospinel $MnSc_2S_4$ induced by a magnetic field, where geometric frustration and anisotropy seem to play the key role [35].

In this paper, we demonstrate that frustrated Mott insulators coupled to a superlattice of nonmagnetic impurities can generate chiral states in the presence of an external magnetic field. In contrast to Ref. [36], where we have shown that a single nonmagnetic impurity nucleates a magnetic vortex over a finite range of magnetic field values above the bulk saturation field H_{sat}, here we focus on the effects of a *periodic array* of nonmagnetic impurities *below* the saturation field. A crucial observation is that the local saturation field H_{sat}^I around an impurity can be higher than H_{sat} in frustrated magnets with competing ferromagnetic and antiferromagnetic interactions. Given that a single impurity nucleates a magnetic vortex around it for $H_{sat} < H < H_{sat}^I$, it is natural to ask about the effect of an array of impurities when $H < H_{sat}$. It is known that nonmagnetic impurities tend to reorient the surrounding spins into a less collinear fashion by inducing an effective biquadratic interaction $(\mathbf{S}_j \cdot \mathbf{S}_k)^2$ with a positive (hence antiferroquadrupolar) coupling constant [37–40]. This rather general observation provides an alternative motivation for studying the magnetic effects of periodic, and nearly periodic, arrays of impurities.

Motivated by these observations, we focus on the low-temperature (T) physics of a classical spin model. An important prerequisite is to include competing ferromagnetic and antiferromagnetic exchange interactions so that the Fourier transform $J(\mathbf{q})$ has multiple degenerate minima $\mathbf{Q}_1, \mathbf{Q}_2, \ldots$ connected by lattice symmetry transformations. The ordered array of nonmagnetic impurities may be realized in a

hole- or electron-doped system with sufficiently strong off-site Coulomb interactions so that a charge density wave (CDW) order leads to an array of holes or doubly occupied sites. For instance, certain high-T_c superconductors and related materials are known to have a CDW of holes at a hole concentration $x = \frac{1}{8}$ (Refs. [41,42]). Other possible realizations will be discussed later.

The rest of the paper is organized as follows. In Sec. II, we present our model, outline our Monte Carlo (MC) method, and list the observables that we evaluate. In Sec. III, we show the temperature (T)-magnetic field (H) phase diagram for a perfectly periodic array of nonmagnetic impurities and a simple relation between the superlattice reciprocal unit vectors and the Q vectors (a preliminary account of the discussion in Sec. III A was presented in Ref. [43]). A plethora of multiple-Q phases are obtained from our MC simulations. In Sec. IV, we provide a variational analysis that explains all of the numerically obtained phases close to $T = 0$. In Sec. V, we discuss the effects of changing the impurity concentration or introducing small quenched randomness to the impurity lattice. Section VI includes a discussion of potential realizations of periodic arrays of nonmagnetic impurities.

II. MODEL

A. Model

We consider a two-dimensional classical J_1-J_3 triangular-lattice Heisenberg magnet in a magnetic field with nonmagnetic impurities. In the absence of impurities, the Hamiltonian is

$$\mathcal{H}_{\text{pure}} = J_1 \sum_{\langle j,l \rangle} \mathbf{S}_j \cdot \mathbf{S}_l + J_3 \sum_{\langle\langle j,l \rangle\rangle} \mathbf{S}_j \cdot \mathbf{S}_l - H \sum_j S_j^z. \quad (1)$$

In order to realize $H_{\text{sat}} < H_{\text{sat}}^I$, we adopt ferromagnetic nearest-neighbor (NN) exchange $J_1 < 0$ and antiferromagnetic third-NN exchange $J_3 > 0$. Note that the qualitative features derived from the J_1-J_3 model, such as $H_{\text{sat}} < H_{\text{sat}}^I$ and the presence of more than one symmetry related ordering wave vectors [see Eq. (4)], are expected to hold for a broad class of frustrated Heisenberg magnets. $\mathbf{S}_j$ represents a classical spin located at the site j with $|\mathbf{S}_j| = 1$. The thermodynamic phase diagram of this model Hamiltonian includes a magnetic-field-induced finite-temperature skyrmion crystal phase [21,23–25] for

$$J_3/|J_1| > J_3^c/|J_1| = 1.0256(53). \quad (2)$$

The skyrmion crystal is a state with spontaneously broken chiral symmetry, corresponding to the superposition of harmonic waves with sixfold-degenerate incommensurate wave vectors $\pm\mathbf{Q}_\nu$ ($\nu = 1$–3). These are the wave vectors that minimize the Fourier transform of the exchange interaction

$$J(\mathbf{q}) = \sum_{1 \leqslant j \leqslant 3} (J_1 \cos \mathbf{q} \cdot \mathbf{e}_j + J_3 \cos 2\mathbf{q} \cdot \mathbf{e}_j). \quad (3)$$

Here, $\mathbf{e}_1 = \hat{\mathbf{x}}$, $\mathbf{e}_2 = -\hat{\mathbf{x}}/2 + \sqrt{3}\hat{\mathbf{y}}/2$, and $\mathbf{e}_3 = -\mathbf{e}_1 - \mathbf{e}_2$. The incommensurate minima emanate from the Γ point (Lifshitz

transition) for $J_3/|J_1| > \frac{1}{4}$,

$$
\begin{aligned}
\pm\mathbf{Q}_1 &= \pm Q\hat{\mathbf{x}}, \\
\pm\mathbf{Q}_2 &= \pm Q(-\hat{\mathbf{x}}/2 + \sqrt{3}\hat{\mathbf{y}}/2), \quad (4) \\
\pm\mathbf{Q}_3 &= \pm Q(-\hat{\mathbf{x}}/2 - \sqrt{3}\hat{\mathbf{y}}/2),
\end{aligned}
$$

with

$$Q = 2 \arccos\left[\frac{1}{4}\left(1 + \sqrt{1 - \frac{2J_1}{J_3}}\right)\right], \quad (5)$$

where the lattice spacing is $a = a^{-1} = 1$ in our convention. Thus, according to Eqs. (2) and (5), the skyrmion crystal phase is only stable for $Q/(2\pi) > Q_c/(2\pi) = 0.2623(3)$. For $|J_1|/4 < J_3 \lesssim J_3^c$, $J(\mathbf{q})$ resembles the bottom of a wine bottle near the Γ point, with a weaker C_6 anisotropy as the system approaches the Lifshitz transition point $J_3 = |J_1|/4$. In this regime, the phase diagram comprises only the high-temperature paramagnetic phase and the single-Q conical spiral phase, both of which have no net scalar spin chirality [25].

We will first consider the effect of a periodic array of non-magnetic impurities forming a perfect triangular superlattice. The primitive reciprocal superlattice vectors are

$$\mathbf{K}_\pm = \frac{2\pi}{a_{\text{imp}}}(1, \pm 1/\sqrt{3}), \quad (6)$$

where a_{imp} is the impurity superlattice constant. The impurities are introduced in the Hamiltonian by replacing

$$\mathbf{S}_j \to p_j \mathbf{S}_j, \quad (7)$$

where $p_j = 0$ (1) for a nonmagnetic impurity (magnetic) site. This amounts to introducing the impurity contribution to the Hamiltonian $\mathcal{H}_{\text{imp}} = \mathcal{H}_{\text{imp}}^J + \mathcal{H}_{\text{imp}}^H$, so that

$$\mathcal{H} = \mathcal{H}_{\text{pure}} + \mathcal{H}_{\text{imp}}^J + \mathcal{H}_{\text{imp}}^H, \quad (8)$$

with

$$
\begin{aligned}
\mathcal{H}_{\text{imp}}^J &= -\sum_j (1 - p_j) \sum_\eta J_{j,\eta} \mathbf{S}_j \cdot \mathbf{S}_{j+\eta}, \\
\mathcal{H}_{\text{imp}}^H &= H \sum_j (1 - p_j) S_j^z.
\end{aligned}
\quad (9)
$$

Here, η is the index of the coordination vectors and the different notation $J_{j,\eta} = J_1, J_3$ for the exchange coupling is associated with the ηth coordination vector at each site j. After presenting phase diagrams for periodic arrays of impurities (Sec. III), we will introduce a small randomness in the impurity locations around the superlattice sites (Sec. V B).

B. Monte Carlo method

We perform classical MC simulations of our spin Hamiltonian $\mathcal{H}$ given in Eq. (8) for several impurity configurations to be specified below. Our simulations are carried out with the standard Metropolis local updates supplemented with the over-relaxation method [44]. The lattice has $N = L^2$ sites (including impurity sites) with $L = 48, 64, 72, 80$, and 96 and we impose the periodic boundary conditions in both directions. We first perform simulated annealing for 10^5–10^6

MC sweeps (MCS) to find low-energy configuration, which is then followed by equilibration steps and a subsequent sampling process of 10^5–10^7 MCS at the target temperature. The statistical errors are estimated from 5–64 independent runs.

We calculate the specific heat C, the uniform magnetic susceptibility dM/dH, and the spin and the chirality structure factors. The spin structure factor $S_s^{\alpha\alpha}(\mathbf{q})$ ($\alpha = x,y,z$) is given by

$$S_s^{\alpha\alpha}(\mathbf{q}) = \frac{1}{N} \sum_{j,l} \langle S_j^\alpha S_l^\alpha \rangle e^{i\mathbf{q}\cdot(\mathbf{r}_j - \mathbf{r}_l)},$$

$$S_s^\perp(\mathbf{q}) = S_s^{xx}(\mathbf{q}) + S_s^{yy}(\mathbf{q}). \tag{10}$$

We define the chirality structure factor $S_\chi^\mu(\mathbf{q})$ for the upward and downward triangles ($\mu = u,d$, respectively) as

$$S_\chi^\mu(\mathbf{q}) = \frac{1}{N} \sum_{\mathbf{R},\mathbf{R}'\in\mu} \langle \chi_\mathbf{R} \chi_{\mathbf{R}'} \rangle e^{i\mathbf{q}\cdot(\mathbf{R}-\mathbf{R}')}, \tag{11}$$

where $\mathbf{R},\mathbf{R}'$ run over sites of the specified sublattice, $\mu = u,d$, of the dual honeycomb lattice. $\chi_\mathbf{R} = \mathbf{S}_j \cdot (\mathbf{S}_k \times \mathbf{S}_l)$ is the spin scalar chirality associated with a triangle centered at $\mathbf{R}$, where j,k,l are the sites aligned counterclockwise on the triangle. We also introduce the following notations for the total scalar chirality associated with the up (χ^u) and the down (χ^d) triangles

$$\chi^\mu = \frac{1}{N} \sum_{\mathbf{R}\in\mu} \chi_\mathbf{R} \quad \text{for} \quad \mu = u,d, \tag{12}$$

and their sum

$$\chi^{\text{tot}} = \chi^u + \chi^d, \tag{13}$$

which is the total scalar chirality.

III. PERIODIC ARRAY OF IMPURITIES

We start our discussion with the case where magnetic impurities form a perfect triangular superlattice. We first require commensurability between the superlattice reciprocal vectors $\mathbf{K}_\pm$ and $\pm\mathbf{Q}_{1\leqslant\nu\leqslant 3}$, which is expected to enhance the constructive interference between the impurity superlattice and the spin texture (we will relax this condition later). For the sake of concreteness, we fix $J_3/|J_1| = 1/(4-2\sqrt{2}) \approx 0.854$ unless otherwise specified, which corresponds to $Q/(2\pi) = \frac{1}{4}$ according to Eq. (5). Given that $J_3 < J_3^c$, the phase diagram in absence of impurities only includes the single-Q conical spiral state shown in Fig. 2(b). Such a state is not chiral because χ^u and χ^d cancel each other. For nonzero H, this quasi-long-range ordered state completely breaks the C_6 symmetry of $\mathcal{H}$ because of the associated bond ordering, whereas the C_6 symmetry is broken down to C_3 for $H = 0$ as there is a continuous symmetry operation that can change the sign of the vector chirality. In both cases, our results are consistent with the single-step first-order transition found for the zero-field J_1-J_3 model with classical XY and Heisenberg spins in Refs. [45–47], where the symmetry is O(2) and O(3), respectively, corresponding to the cases with and without the magnetic field in the present consideration.

As described in the Introduction, the nonmagnetic impurities in a frustrated magnet with competing ferromagnetic and
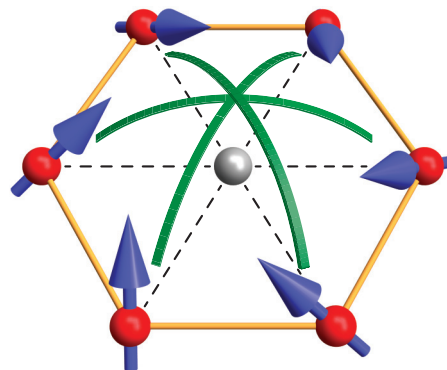

FIG. 1. Schematic picture for a local configuration in a magnetic field around a nonmagnetic impurity (at the center). The straight solid (dashed) lines represent the remaining (removed) ferromagnetic exchange J_1 interactions. The arc lines represent the antiferromagnetic exchange J_3.

antiferromagnetic exchanges make the local saturation field for the surrounding spins larger than the bulk value ($H_{\text{sat}}^I > H_{\text{sat}}$). This is so because the nearest-neighbor spins of the nonmagnetic impurity feel a molecular field, whose component parallel to the applied field is lower than the average for other spins. This effect is of course present for any value of the external field: the spins that surround a nonmagnetic impurity have a lower magnetic susceptibility because the impurity removes the ferromagnetic (J_1) bonds connecting them to the missing spin (Fig. 1). Because the field inducing the z spin component for these spins is smaller than the average, their xy component becomes larger at low energies. Moreover, we can anticipate that the resulting local spin configuration near each impurity is likely to be a vortex as in the case with $H_{\text{sat}} < H < H_{\text{sat}}^I$ [36] because of the competition between J_1 and J_3 for the six spins surrounding the impurity (Fig. 1). The rest of the spins have to accommodate their configuration to the local "boundary condition" imposed by each impurity.

Below, we consider two representative cases where the superlattice constant for the periodic impurities is $a_{\text{imp}} = 8$ and 4. They correspond to simple relations between the superlattice reciprocal vectors and the Q vectors, namely, $\mathbf{K}_+ + \mathbf{K}_- = \mathbf{Q}_1$ and $\mathbf{K}_+ + \mathbf{K}_- = 2\mathbf{Q}_1$, respectively. We will demonstrate that such a commensurate impurity superlattice produces a drastic change of the magnetic phase diagram. Our finite-size scaling analysis to characterize the phases is summarized in Appendix.

A. Case with $a_{\text{imp}} = 8$

The configuration of impurities is shown in the inset of Fig. 2(a). The impurities are separated by $a_{\text{imp}} = 8$ sites along the lattice principal directions. This superlattice spacing is exactly twice as large as $2\pi/Q = 4$.

Figure 2(a) shows the T-H phase diagram obtained with our MC simulations, which features eight different phases other than the paramagnetic state (Table I). The phase boundaries are determined by analyzing the structure factors in Eqs. (10) and (11) (Figs. 3 and 4) and the peak in the uniform magnetic susceptibility [Fig. 2(d)] as a function of H. Notably, many phases are multiple-Q states that support
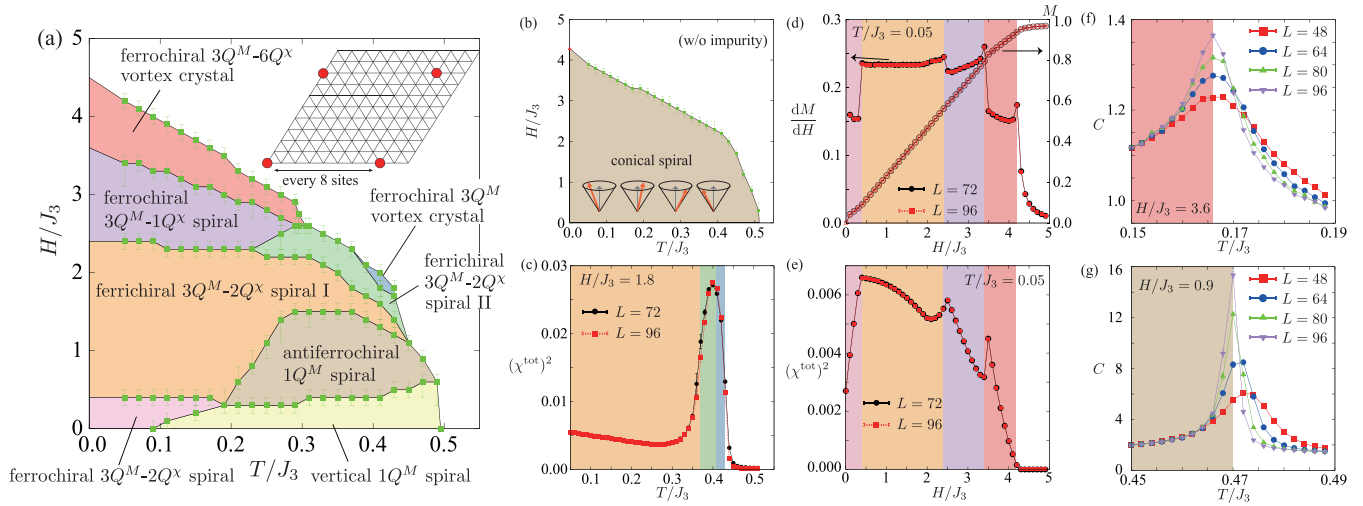
FIG. 2. (a) Phase diagram for a perfect periodic array of impurities ($a_{\rm imp} = 8$) with $J_3/|J_1| \approx 0.854$ ($Q = 2\pi/4$). The inset shows the impurity superlattice. (b) Phase diagram of $\mathcal{H}_{\rm pure}$. (c) T dependence of the net scalar chirality at $H/J_3 = 0.18$, (d) magnetization curve and its H derivative at $T/J_3 = 0.05$, and (e) H dependence of $(\chi^{\rm tot})^2$ at $T/J_3 = 0.05$, for the model including a periodic array of impurities. (f), (g) T dependence of the specific heat at (f) $H/J_3 = 3.6$ and (g) $H/J_3 = 0.9$.

long-wavelength modulation of local scalar chirality (chirality wave), which is not necessarily single-Q^χ but some of them are actually of the multiple-Q^χ type (our convention is to use Q^M and Q^χ, respectively, when it is necessary to make an unambiguous distinction between spin and chirality textures). The commensuration between the chirality waves and the impurity superlattice leads to a majority of magnetically ordered phases with net scalar spin chirality [see Figs. 2(c) and 2(e)]. The uniform component arises from uncompensated positive and negative components of the chirality wave texture: the impurities remove spins contributing to only one sign of the modulated chiral structure. Meanwhile, the xy spin

components only exhibit quasi-long-range correlations in $d = 2$, as expected from Mermin-Wagner's theorem [48]. In agreement with our discussion above, the spins around the impurities form vortices with enhanced xy components. In what follows, we describe details of the obtained phases.

a. Ferrochiral $3Q^M$-$6Q^\chi$ vortex crystal.[1] This phase appears right below the saturation field near $T = 0$. Upon

---

[1]In our convention, we count the number of pairs $\pm Q^M$ and $\pm Q^\chi$ corresponding to the (quasi-)Bragg peaks in the structure factor.

TABLE I. Classification of the ordered phases in the classical J_1-J_3 Heisenberg model with periodic nonmagnetic impurities. Here, $J_3/|J_1| \approx 0.854$ and the period of the impurity superlattice is $a_{\rm imp} = 8$. From the fourth to the sixth column, our notation of "$n + n_{\rm sub}(+n'_{\rm sub})$" means that the corresponding structure factor has n dominant peaks as well as $n_{\rm sub}$ subdominant (and $n'_{\rm sub}$ even smaller) peaks.

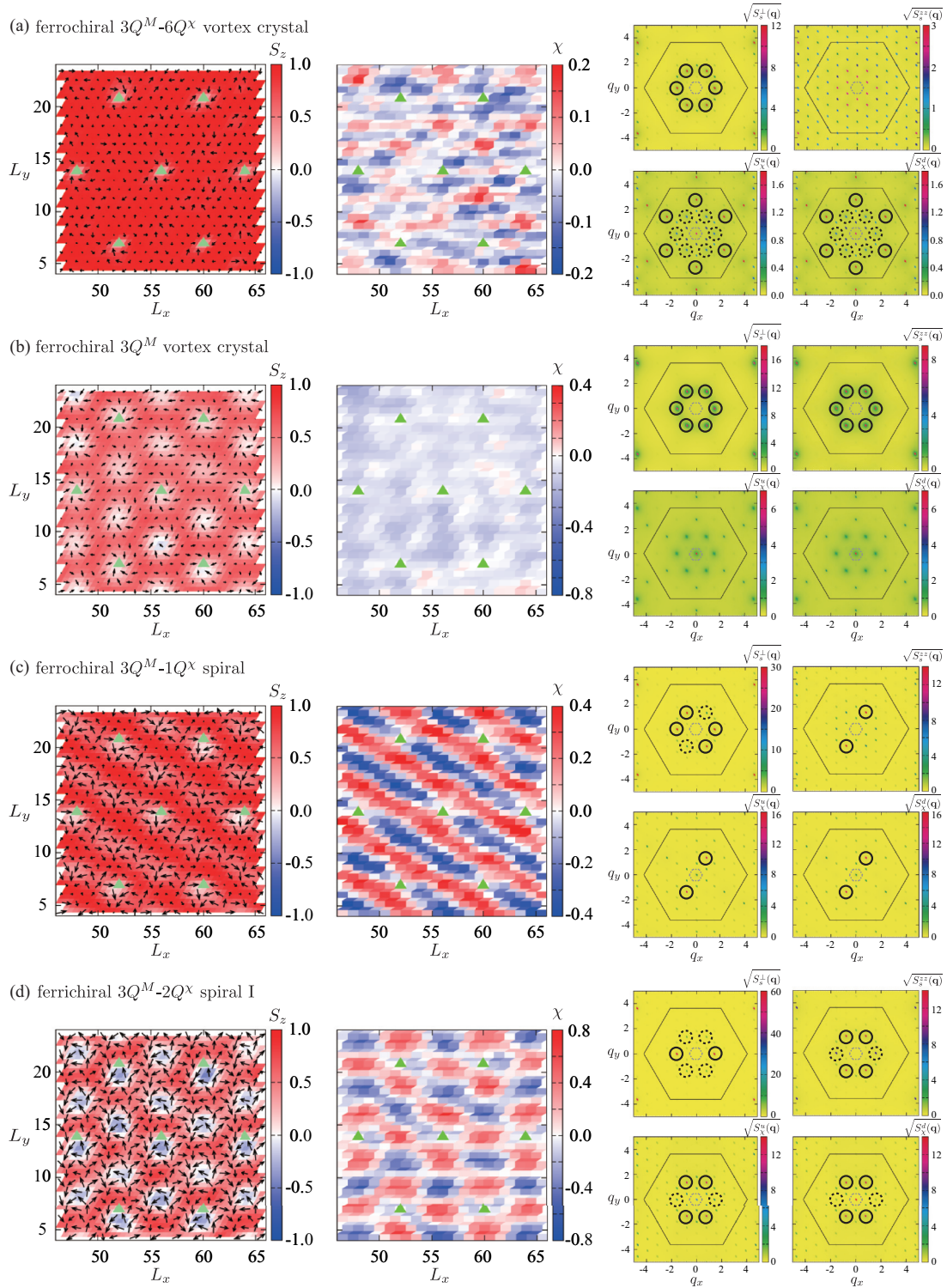| Phase	Nonzero net scalar chirality	Chirality of up and down triangles	Number of (quasi-)Bragg peaks in $S_s^\perp(\mathbf{Q})$	Number of (quasi-)Bragg peaks in $S_s^{zz}(\mathbf{Q})$ at $\mathbf{q} \neq 0$	Number of Bragg peaks in $S_\chi^{u/d}(\mathbf{Q})$ at $\mathbf{q} \neq 0$	Broken point-group symmetry (of the lattice with impurities)
Ferrochiral $3Q^M$-$6Q^\chi$ vortex crystal	✓	$\chi^u = \chi^d$	3	0	3+3	
Ferrochiral $3Q^M$ vortex crystal	✓	$\chi^u = \chi^d$	3	3	0	
Ferrochiral $3Q^M$-$1Q^\chi$ spiral	✓	$\chi^u = \chi^d$	2+1	1	1	C_6
Ferrichiral $3Q^M$-$2Q^\chi$ spiral I	✓	$|\chi^u| \neq |\chi^d|$	1+2	2+1	2+1	C_6
Ferrichiral $3Q^M$-$2Q^\chi$ spiral II	✓	$|\chi^u| \neq |\chi^d|$	1+1+1	1+1+1	1+1+1	C_6
Antiferrochiral $1Q^M$ spiral	No	$\chi^u = -\chi^d$	1	1	0	C_6
Ferrochiral $3Q^M$-$2Q^\chi$ spiral	✓	$\chi^u = \chi^d$	1+2	1	2+1	C_6
Vertical $1Q^M$ spiral	No		1	1	0	C_6 (C_3 for $H = 0$)

FIG. 3. Snapshots of the spin (left) and the chirality (middle) configurations in the ordered phases for $J_3/|J_1| \approx 0.854$ ($Q = 2\pi/4$) when periodic impurities (triangles) with $a_{\mathrm{imp}} = 8$ are present. The spin and the chirality structure factors are shown on the right: (a) ferrochiral $3Q^M$-$6Q^\chi$ vortex crystal ($H/J_3 = 4.0$ and $T/J_3 = 0.05$), (b) ferrochiral $3Q^M$ vortex crystal ($H/J_3 = 1.9$ and $T/J_3 = 0.41$), (c) ferrochiral $3Q^M$-$1Q^\chi$ spiral ($H/J_3 = 3.0$ and $T/J_3 = 0.05$), and (d) ferrichiral $3Q^M$-$2Q^\chi$ spiral I ($H/J_3 = 1.5$ and $T/J_3 = 0.05$). The circles with solid (dashed) lines indicate the dominant (subdominant) $\mathbf{q} \neq 0$ peak(s). Note that the $\mathbf{q} = 0$ component is removed from $S_s^{zz}(\mathbf{q})$. The hexagon with a solid (dashed) line shows the first Brillouin zone (of the impurity superlattice). To obtain the smooth spin configurations, we integrate out short-wavelength fluctuations by averaging over 50–500 MCS.
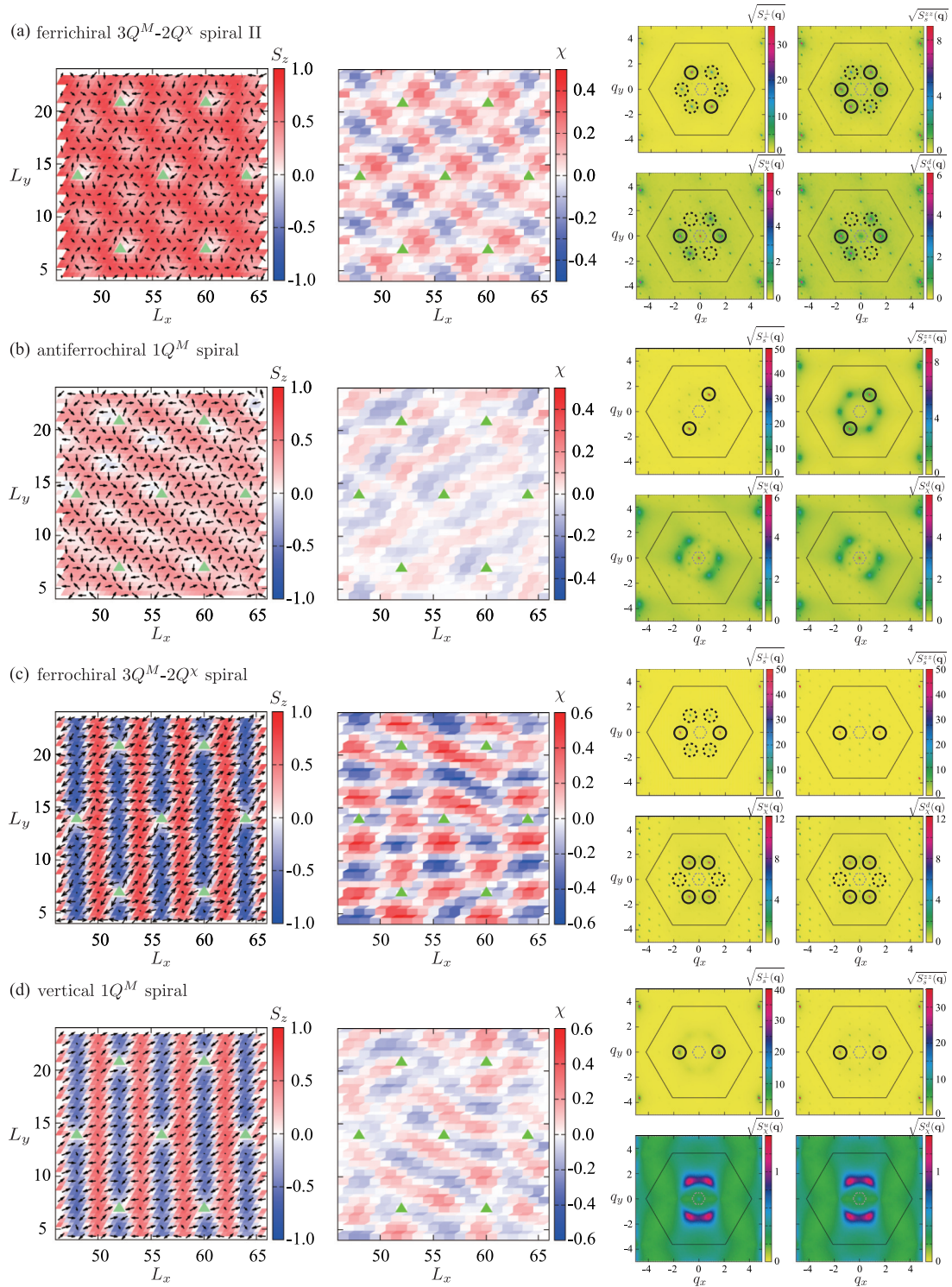
FIG. 4. Snapshots of the spin (left) and the chirality (middle) configurations in the ordered phases for $J_3/|J_1| \approx 0.854$ ($Q = 2\pi/4$) when periodic impurities (triangles) with $a_{\text{imp}} = 8$ are present. The spin and the chirality structure factors are shown on the right: (a) ferrichiral $3Q^M$-$2Q^\chi$ spiral II ($H/J_3 = 2.2$ and $T/J_3 = 0.35$), (b) antiferrochiral single-Q^M spiral ($H/J_3 = 1.0$ and $T/J_3 = 0.35$), (c) ferrochiral $3Q^M$-$2Q^\chi$ spiral ($H/J_3 = 0.1$ and $T/J_3 = 0.05$), and (d) vertical single-Q^M spiral ($H/J_3 = 0.2$ and $T/J_3 = 0.35$). The circles with solid (dashed) lines indicate the dominant (subdominant) $\mathbf{q} \neq 0$ peak(s). Note that the $\mathbf{q} = 0$ component is removed from $S_s^{zz}(\mathbf{q})$. The hexagon with a solid (dashed) line shows the first Brillouin zone (of the impurity superlattice). To obtain the smooth spin configurations, we integrate out short-wavelength fluctuations by averaging over 50–500 MCS.

entering this phase via the thermal transition, the specific heat shows a single weak anomaly as shown in Fig. 2(f). The spin configuration is a triple-Q^M vortex crystal similar to the one reported recently in three-dimensional (3D) frustrated quantum magnets [26,27]. This phase may be understood as the natural extension of the single-impurity vortex for $H_{sat} < H < H_{sat}^I$ [36]. In fact, as shown in Fig. 3(a), each nonmagnetic impurity induces a vortex very similar to the schematic picture in Fig. 1, forming a triangular vortex lattice as a whole. Upon closer inspection, it is possible to see that antivortices appear right in the middle of nearest-neighbor vortices, so that the "boundary condition" by the impurity array is satisfied. The vortices and antivortices give opposite contributions to the scalar spin chirality. While this would lead to a total cancellation of χ^{tot} in a system without impurities [26], the present vortex crystal has net scalar spin chirality because the local scalar chirality around each impurity has the same sign. The net chirality for up and down triangles is equal, $\chi^u = \chi^d$, which we refer to as "ferrochiral." Interestingly, the chirality wave is primarily characterized by higher harmonics relative to the wave vectors that minimize $J(\mathbf{q})$, namely, $\mathbf{Q}_1^\chi = \mathbf{Q}_1 + 2\mathbf{Q}_2$, etc.

b. Ferrochiral $3Q^M$ vortex crystal. This phase can be seen as another type of crystallization of vortices found in Ref. [36] for $H_{sat} < H < H_{sat}^I$. It occupies a small corner of the entire region of the ordered phases, which appears right below the saturation field in the range of intermediate temperature, $0.37 \lesssim T/J_3 \lesssim 0.43$. The spin configuration is characterized by the triple-Q^M modulation and net spin scalar chirality ($\chi^u = \chi^d \neq 0$) [Fig. 3(b)]. However, unlike the ferrochiral $3Q^M$-$6Q^\chi$ vortex crystal phase discussed above, the chirality texture does not support a static finite-Q^χ component in the thermodynamic limit (namely, the chirality texture is homogeneous) as shown in Fig. 14(b) in Appendix; this aspect distinguishes this phase from the skyrmion crystal phase [21], although both phases are triple-Q^M and chiral. Moreover, the z component near the impurities is $S^z \sim 0$ in the ferrochiral $3Q^M$ vortex crystal phase, while it is $S^z \sim -1$ in the skyrmion crystal phase, which implies a different topological nature. The scalar chirality shows a peak near the phase boundary between this and the ferrichiral $3Q^M$-$2Q^\chi$ spiral II phase discussed below [Fig. 2(c)].

c. Ferrochiral $3Q^M$-$1Q^\chi$ spiral. This phase occupies a smaller-H region next to the ferrochiral $3Q^M$-$6Q^\chi$ vortex crystal phase at low T. As shown in Fig. 3(c), it has a triple-Q^M spin texture. In the structure factor for the xy component, there are two dominant peaks and a single subdominant peak, while a single-Q peak is in the structure factor for the z component. Upon closer looking, it becomes clear that the spin texture is pinned by the impurities via the parts with local chirality having the same sign; for this reason, this state is chiral, $\chi^u = \chi^d \neq 0$. In addition to the uniform component, the chirality texture has a single-Q^χ component corresponding to the stripe modulation.

d. Ferrichiral $3Q^M$-$2Q^\chi$ spiral I. This phase occupies the largest portion of the phase diagram among the ordered phases and it is found next to the ferrochiral $3Q^M$-$1Q^\chi$ spiral upon decreasing H. The spin configuration is characterized by the triple-Q^M noncoplanar modulation. $S_s^{zz}(\mathbf{q})$ has two dominant peaks with an additional smaller peak, which in

$S_s^\perp(\mathbf{q})$ in turn correspond to two subdominant peaks and the major peak, respectively [Fig. 3(d)]. We find that the impurities are on the contour $S^z \approx 0$ as shown in the left panel of Fig. 3(d) in accordance with the general argument that the effect of the magnetic field is effectively weakened for spins surrounding impurities. The chirality wave is mainly characterized by the double-Q^χ modulation, which can be seen as the "checkerboard" pattern. Note that the ferrichiral $3Q^M$-$2Q^\chi$ spiral I phase also possesses a small subdominant peak at $\mathbf{Q}_1 + \mathbf{Q}_2$ as shown in the chiral structure factor in Fig. 3(d). A subtle difference is that $S_\chi^u(\mathbf{q})$ and $S_\chi^d(\mathbf{q})$ have different profiles in this state. Based on this observation, we call this state "ferrichiral."

e. Ferrichiral $3Q^M$-$2Q^\chi$ spiral II. This state is found in the intermediate-H regime, next to the ferrichiral $3Q^M$-$2Q^\chi$ spiral I phase upon increasing T. While this is very similar to the ferrichiral $3Q^M$-$2Q^\chi$ spiral I, the intensities of the two dominant components of the chiral structure factor are different in this phase [Fig. 4(a)], while the ones for the ferrichiral $3Q^M$-$2Q^\chi$ spiral I phase are the same.

f. Antiferrochiral single-Q^M spiral. This state appears next to the ferrichiral $3Q^M$-$2Q^\chi$ spiral II state upon decreasing H. The spin configuration shown in Fig. 4(b) resembles the conical spiral state that is obtained without impurities [Fig. 2(b)]. The difference, however, is that the impurities introduce the additional weak longitudinal modulation. The C_6 symmetry is broken in this phase as in the single-Q spiral phase in the pure J_1-J_3 model with easy-plane anisotropy, where the symmetry of the global spin rotation, U(1), is the same as in the present case [46]. The obtained specific-heat curve [Fig. 2(g)] is consistent with the single first-order phase transition reported by Tamura *et al.* [46] in the pure easy-plane model, although a more careful finite-size scaling is required to settle this point. This state is not chiral because χ^u and χ^d cancel each other out: $\chi^u = -\chi^d$. For this reason, we refer to this phase as "antiferrochiral."

g. Ferrochiral $3Q^M$-$2Q^\chi$ spiral. This phase occupies the low-field and low-T region of the phase diagram [Fig. 2(a)] and appears next to the ferrichiral $3Q^M$-$2Q^\chi$ spiral I phase with decreasing H. The spin configuration [see Fig. 4(c)] closely resembles a single-Q^M vertical spiral state (see below) although the small additional Q^M components render the spin configuration noncoplanar with the triple-Q^M modulation. Meanwhile, the chirality wave texture shows the double-Q^χ modulation with a single-Q^χ subdominant component, which is very similar to that of the ferrichiral $3Q^M$-$2Q^\chi$ spiral I state. The difference is that the net chirality for up and down triangles in the present state is equal, $\chi^u = \chi^d$, while it is different in the ferrichiral $3Q^M$-$2Q^\chi$ spiral state. Once again, it is evident that the spin texture is pinned by the impurities where the local chirality has the same sign, which leads to nonzero uniform scalar chirality. The ferrochiral $3Q^M$-$2Q^\chi$ spiral state extends its stability down to $H = 0$, as shown in Fig. 2(e).

h. Vertical single-Q^M spiral. This phase occupies a region at higher T next to the ferrochiral $3Q^M$-$2Q^\chi$ spiral phase. This is a single-Q^M coplanar state in an arbitrary plane containing the vertical c axis when the magnetic field is applied in the c direction. Thus, this state has no net chirality. The difference relative to the ferrochiral $3Q^M$-$2Q^\chi$ spiral state is the disappearance of the subdominant components in the spin
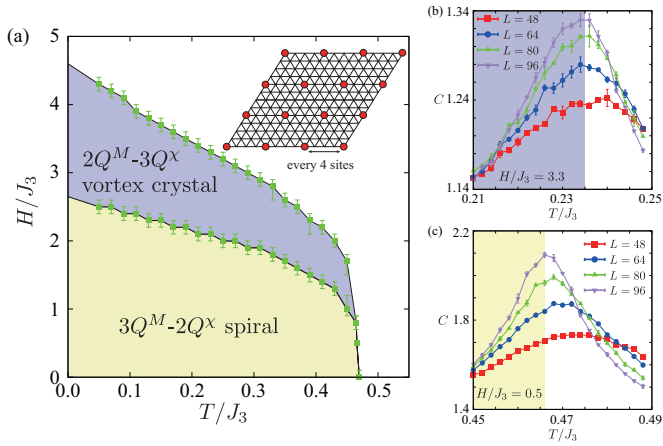
FIG. 5. (a) Phase diagram of the model with a periodic array of impurities with $a_{\mathrm{imp}} = 4$ and $J_3/|J_1| \approx 0.854$ ($Q = 2\pi/4$). The inset shows the impurity configuration. (b), (c) T dependence of the specific heat at (b) $H/J_3 = 3.3$ and (c) $H/J_3 = 0.5$.

structure factor induced by thermal fluctuations [Fig. 4(d)]. The transition from the paramagnetic state is suggested to be a single-step first-order phase transition (not shown). This is similar to the case in the pure J_1-J_3 model [45–47], albeit with a subtle difference that the state in the latter is the conical spiral.

B. Case with $a_{\mathrm{imp}} = 4$

Next, we briefly discuss the case where the superlattice constant $a_{\mathrm{imp}} = 4$ is half of the previous case, as illustrated in the inset of Fig. 5(a). This corresponds to the relation $\mathbf{K}_+ + \mathbf{K}_- = 2\mathbf{Q}_1$. Even though the commensurability still holds, the obtained phases summarized in Table II are very different from the previous case, except for the fact that a vortex crystal still appears right below the saturation field.

a. Nonchiral $2Q^M$-$3Q^\chi$ vortex crystal. As it is shown in Fig. 6(a), the high-field state is another vortex crystal, in which both the vortices and antivortices are nucleated by the impurities. The vortex and antivortex chains alternate, creating the stripe pattern shown in the middle of Fig. 6(a). This stripe pattern breaks the translational symmetry of the system. Vortices and antivortices have opposite scalar spin chirality, producing a chirality wave with a wave vector equal to half of the impurity lattice reciprocal vector: $\mathbf{Q}^\chi = \mathbf{K}^+/2$ [Fig. 6(a)]. Given that both vortex structures, the vortices and the antivortices, are nucleated around the impurities, the net chirality is perfectly canceled, rendering this state nonchiral.

Figure 5(b) shows the specific curve heat near the thermal phase transition. Although it is suggestive of a single-step continuous phase transition, a more careful analysis will be required to draw a final conclusion about the critical behavior.

b. Nonchiral $3Q^M$-$2Q^\chi$ spiral. The spin configuration in the low-field phase has a single-Q^M longitudinal modulation and a double-Q^M transverse modulation [Fig. 6(b)]. A closer inspection reveals that both $S_s^\perp(\mathbf{q})$ and $S_s^{zz}(\mathbf{q})$ have additional peaks induced by the impurities, such as the peaks at $q = \pi/\sqrt{3} \approx 1.814$ and $\pi/(2\sqrt{3}) \approx 0.907$. This fact is more evident for the double-Q^χ chirality wave texture, in which the subdominant component is induced by the impurities. The spin configuration accommodates itself to the impurity superlattice in such a way that the impurities are on the nodal line of the chirality wave texture [Fig. 6(b)]. As depicted in Fig. 6(b), the net chirality vanishes. The specific heat near the thermal phase transition is suggestive of a single-step continuous phase transition also in this case [Fig. 5(c)].

IV. VARIATIONAL ANALYSIS

Our numerical calculation indicates that multiple-Q ground states are realized instead of the single-Q conical ground state that is obtained for the pure system. Below, we provide a variational analysis confirming that the commensurability relation between the Q vectors and the superlattice reciprocal vectors $\mathbf{K}_\pm$ renders the single-Q conical state unstable towards more complex multiple-Q structures. For the sake of concreteness, we consider below the case $a_{\mathrm{imp}} = 8$ where $\mathbf{K}_+ + \mathbf{K}_- = \mathbf{Q}_1$.

First we note that $\mathcal{H}_{\mathrm{imp}}^J$ in Eq. (9) can be written as

$$\mathcal{H}_{\mathrm{imp}}^J = -\rho_{\mathrm{imp}} \sum_{\mathbf{q},\mathbf{q}' \in \mathrm{FBZ}} 2J(\mathbf{q}) \left(\sum_{\mathbf{G}_{\mathrm{imp}}} \delta_{\mathbf{q}',\mathbf{q}+\mathbf{G}_{\mathrm{imp}}} \right) \mathbf{S}_\mathbf{q} \cdot \mathbf{S}_{-\mathbf{q}'},$$
(14)

after taking the Fourier transform $\mathbf{S}_\mathbf{q} = \sqrt{1/N} \sum_j e^{-i\mathbf{q}\cdot\mathbf{r}_j} \mathbf{S}_j$. $\mathbf{G}_{\mathrm{imp}}$ runs over the set of impurity superlattice reciprocal vectors and $\rho_{\mathrm{imp}} = a_{\mathrm{imp}}^{-2}$ is impurity concentration. Thus, because of the commensurability relation, $\mathcal{H}_{\mathrm{imp}}^J$ couples the different Q vectors and the $\mathbf{q} = 0$ component induced by the magnetic field. Likewise, $\mathcal{H}_{\mathrm{imp}}^H$ is written as

$$\mathcal{H}_{\mathrm{imp}}^H = \sqrt{N} \rho_{\mathrm{imp}} H \sum_{\mathbf{G}_{\mathrm{imp}} \in \mathrm{FBZ}} S_{\mathbf{G}_{\mathrm{imp}}}^z,$$
(15)

where the Q vectors and $\mathbf{q} = 0$ are both included in the summation.

TABLE II. Classification of the ordered phases for $J_3/|J_1| \approx 0.854$ in the model with periodic impurities ($a_{\mathrm{imp}} = 4$).

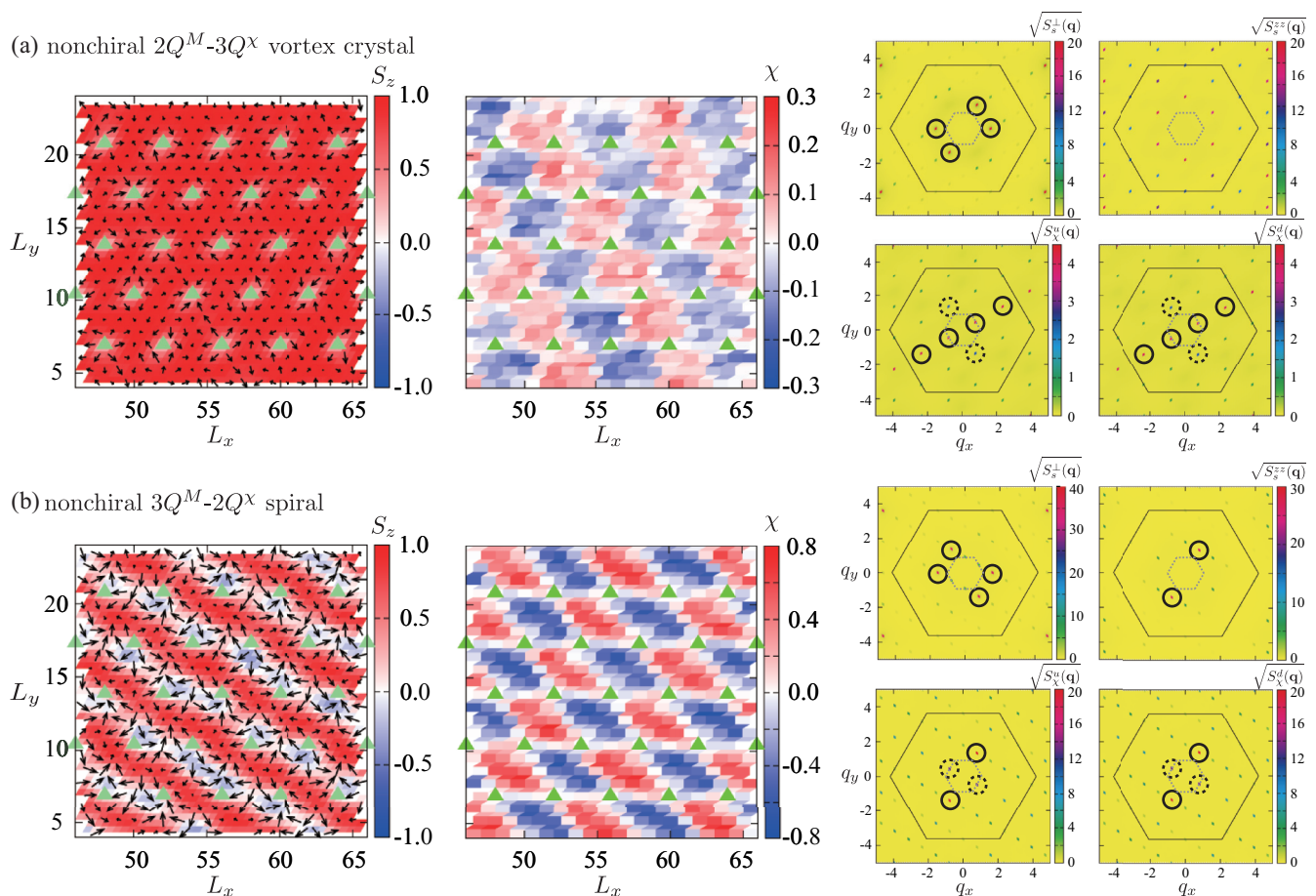| Phase	Nonzero net scalar chirality	Number of (quasi-)Bragg peaks in $S_s^\perp(\mathbf{Q})$	Number of (quasi-)Bragg peaks in $S_s^{zz}(\mathbf{Q})$ at $\mathbf{q} \neq 0$	Number of Bragg peaks in $S_\chi^{u/d}(\mathbf{Q})$ at $\mathbf{q} \neq 0$	Broken point-group symmetry (of the lattice with impurities)
Nonchiral $2Q^M$-$3Q^\chi$ vortex crystal	No	2	0	2+1	C_6
Nonchiral $3Q^M$-$2Q^\chi$ spiral	No	2	1	1+1	C_6

FIG. 6. Snapshots of the spin configuration (left), the chirality texture (middle), and the spin and the chirality structure factors (right) in the model with periodic impurities (triangles) with $a_{\rm imp} = 4$ for $J_3/|J_1| \approx 0.854$ ($Q = 2\pi/4$): (a) nonchiral $2Q^M$-$3Q^\chi$ vortex crystal ($H/J_3 = 3.9$) and (b) nonchiral $3Q^M$-$2Q^\chi$ spiral ($H/J_3 = 1.6$). The circles with solid (dashed) lines indicate the dominant (subdominant) peak(s) at $\mathbf{q} \neq 0$. The $\mathbf{q} = 0$ component is removed from $S_s^{zz}(\mathbf{q})$. The hexagon with a solid (dashed) line shows the first Brillouin zone (of the impurity superlattice). We average over 50–500 MCS to integrate out short-wavelength fluctuations.

A. Stability analysis of the conical spiral

We start from showing that the impurity-induced coupling makes the single-Q state unstable at $T = 0$. To this end, we consider the following deformation of the single-Q conical state, which satisfies the fixed-length constraint required for classical spins:

$$S_j^x = \sqrt{\sin^2 \tilde{\theta} - \delta^2} \cos(\mathbf{Q}_1 \cdot \mathbf{r}_j) + \delta \cos(\mathbf{Q}_2 \cdot \mathbf{r}_j),$$

$$S_j^y = \sqrt{\sin^2 \tilde{\theta} - \delta^2} \sin(\mathbf{Q}_1 \cdot \mathbf{r}_j) - \delta \sin(\mathbf{Q}_2 \cdot \mathbf{r}_j), \quad (16)$$

$$S_j^z = \sqrt{\cos^2 \tilde{\theta} - 2\delta \sqrt{\sin^2 \tilde{\theta} - \delta^2} \cos(\mathbf{Q}_3 \cdot \mathbf{r}_j)},$$

where δ parametrizes the magnitude of the deformation and $\tilde{\theta}$ [which is equal to $\cos^{-1}(S_j^z)$, $\forall j$ for $\delta \to 0$] is a variational parameter. Following Ref. [25], we introduce

$$x = \delta \cos^{-2} \tilde{\theta} \sqrt{\sin^2 \tilde{\theta} - \delta^2}, \quad (17)$$

and S_j^z can be expanded as

$$S_j^z = \cos \tilde{\theta} \sum_{n \geq 0} f_n(x) \cos(n\mathbf{Q}_3 \cdot \mathbf{r}_j), \quad (18)$$

where, to $O(\delta^5)$, $f_0(x) = 1 - x^2/4 - 15x^4/64$, $f_1(x) = -x - 3x^3/8$, $f_2(x) = -x^2/4 - 5x^3/16$, $f_3(x) = -x^3/8$, $f_4(x) = -5x^4/64$, and $f_{n \geq 5}(x)$ can be neglected at this order. We find

$$\langle \mathcal{H}_{\rm imp}^H \rangle = N\rho_{\rm imp} H \cos \tilde{\theta} \left(1 - x - \frac{x^2}{2} - \frac{x^3}{2} - \frac{35x^4}{64} \right)$$
$$+ O(\delta^5). \quad (19)$$

Also, by splitting Eq. (14) into different spin components as $\mathcal{H}_{\rm imp}^J = \mathcal{H}_{\rm imp}^{xx} + \mathcal{H}_{\rm imp}^{yy} + \mathcal{H}_{\rm imp}^{zz}$ and denoting $J_{nQ} = J(n\mathbf{Q}_1) = J(n\mathbf{Q}_2) = J(n\mathbf{Q}_3)$ and $J_0 = J(0)$, we find

$$\langle \mathcal{H}_{\rm imp}^{xx} \rangle = -2N\rho_{\rm imp} J_Q (\sin^2 \tilde{\theta} + 2x \cos^2 \tilde{\theta}),$$
$$\langle \mathcal{H}_{\rm imp}^{yy} \rangle = 0, \quad (20)$$

which are independent of the deformation, and

$$\langle \mathcal{H}_{\text{imp}}^{zz} \rangle = -2N\rho_{\text{imp}} \cos^2 \tilde{\theta} \left[\frac{1}{4} J_0 f_0^2(x) + \frac{1}{2} f_0(x) \sum_{n \geqslant 1} (J_0 + J_{nQ}) f_n(x) + \sum_{n \geqslant 1} J_{nQ} f_n(x) \sum_{m \geqslant 1} f_m(x) \right]$$

$$= -2N\rho_{\text{imp}} \cos^2 \tilde{\theta} \left[\frac{J_0}{4} - \frac{J_0 + J_Q}{2} x - \frac{2J_0 - 8J_Q + J_{2Q}}{8} x^2 + \frac{-2J_0 + 3J_Q + 4J_{2Q} - J_{3Q}}{16} x^3 \right.$$

$$\left. + \frac{-34J_0 + 112J_Q - 8J_{2Q} + 16J_{3Q} - 5J_{4Q}}{128} x^4 \right] + O(\delta^5). \tag{21}$$

These results show that $\langle \mathcal{H}_{\text{imp}} \rangle_\delta - \langle \mathcal{H}_{\text{imp}} \rangle_{\delta=0}$ includes a *linear* contribution in the deformation parameter δ. In the meantime, the change in $\mathcal{H}_{\text{pure}}$ was evaluated in Ref. [25] as $\langle \mathcal{H}_{\text{pure}} \rangle_\delta - \langle \mathcal{H}_{\text{pure}} \rangle_{\delta=0} = N \cos^2 \tilde{\theta} (J_{2Q} - J_0)x^4/32 + O(\delta^5)$. Thus, $\langle \mathcal{H} \rangle_\delta - \langle \mathcal{H} \rangle_{\delta=0}$ decreases linearly in δ, implying that the conical spiral is indeed unstable in the presence of periodic array of impurities commensurate with modulation associated with the ordering wave vectors.

B. Luttinger-Tisza analysis

The next question is whether the numerically found field-induced phases can be analytically explained in a simple manner. Below, we first perform a soft-spin variational analysis at $T = 0$ by adopting the following ansatz:

$$\widetilde{\mathbf{S}}_j = \mathbf{M}_0 + \sum_{1 \leqslant \mu \leqslant 3} (\mathbf{M}_\mu e^{i\mathbf{Q}_\mu \cdot \mathbf{r}_j} + \text{c.c.}), \tag{22}$$

where $\mathbf{M}_0 = N^{-1} \sum_j \widetilde{\mathbf{S}}_j$ is a three-component real vector for the uniform component and $\mathbf{M}_\mu = N^{-1} \sum_j e^{-i\mathbf{Q}_\mu \cdot \mathbf{r}_j} \widetilde{\mathbf{S}}_j$ $(1 \leqslant \mu \leqslant 3)$ are three-component complex vectors. The tilde attached to the spin variable indicates that the fixed-length constraint is replaced by the average normalization condition given by a quadratic function

$$N^{-1} \sum_j |\widetilde{\mathbf{S}}_j|^2 = |\mathbf{M}_0|^2 + 2 \sum_{1 \leqslant \mu \leqslant 3} |\mathbf{M}_\mu|^2 = 1. \tag{23}$$

This average constraint can be easily taken into account with the Lagrange multiplier method.

The variational energy density extended by the Lagrange multiplier λ is $E_{\text{var}} = E_J^{\text{pure}} + E_J^{\text{imp}} + E_H + E_\lambda$ with

$$E_J^{\text{pure}} = J_0 |\mathbf{M}_0|^2 + 2J_Q \sum_{1 \leqslant \mu \leqslant 3} |\mathbf{M}_\mu|^2,$$

$$E_J^{\text{imp}} = -2\rho_{\text{imp}} J_0 |\mathbf{M}_0|^2 - 2\rho_{\text{imp}} J_Q \left| \sum_{1 \leqslant \mu \leqslant 3} (\mathbf{M}_\mu + \mathbf{M}_\mu^*) \right|^2 - 2\rho_{\text{imp}}(J_0 + J_Q) \sum_{1 \leqslant \mu \leqslant 3} \mathbf{M}_0 \cdot (\mathbf{M}_\mu + \mathbf{M}_\mu^*),$$

$$E_H = -(1 - \rho_{\text{imp}}) H M_0^z + \rho_{\text{imp}} H \sum_{1 \leqslant \mu \leqslant 3} \left[M_\mu^z + (M_\mu^z)^* \right],$$

$$E_\lambda = -\lambda \left(|\mathbf{M}_0|^2 + 2 \sum_{1 \leqslant \mu \leqslant 3} |\mathbf{M}_\mu|^2 - 1 \right). \tag{24}$$

By rewriting $\mathbf{M}_0 = \mathbf{A}_0$ and $(\text{Re}\,\mathbf{M}_\mu, \text{Im}\,\mathbf{M}_\mu) = (\mathbf{A}_\mu, \mathbf{B}_\mu)$ for $1 \leqslant \mu \leqslant 3$, we first look into the quadratic part $E_{\text{var}}^{\text{quad}} = E_{\text{var}}(\lambda) - E_H$,

$$E_{\text{var}}^{\text{quad}} = (\mathbf{A}_0 \quad \mathbf{A}_1 \quad \mathbf{A}_2 \quad \mathbf{A}_3) \begin{pmatrix} \omega_0 & \Delta_{0Q} & \Delta_{0Q} & \Delta_{0Q} \\ \Delta_{0Q} & \omega_Q & \Delta_Q & \Delta_Q \\ \Delta_{0Q} & \Delta_Q & \omega_Q & \Delta_Q \\ \Delta_{0Q} & \Delta_Q & \Delta_Q & \omega_Q \end{pmatrix} \begin{pmatrix} \mathbf{A}_0 \\ \mathbf{A}_1 \\ \mathbf{A}_2 \\ \mathbf{A}_3 \end{pmatrix} + 2J_Q \sum_{1 \leqslant \mu \leqslant 3} |\mathbf{B}_\mu|^2$$

$$= \sum_{0 \leqslant \kappa \leqslant 3} \varepsilon_\kappa |\mathbf{\Phi}_\kappa|^2 + 2J_Q \sum_{1 \leqslant \mu \leqslant 3} |\mathbf{B}_\mu|^2, \tag{25}$$

where $\omega_0 = (1 - 2\rho_{\text{imp}})J_0 - \lambda$, $\omega_Q = (2 - 8\rho_{\text{imp}})J_Q - 2\lambda$, $\Delta_{0Q} = -2\rho_{\text{imp}}(J_0 + J_Q)$, and $\Delta_Q = -8\rho_{\text{imp}}J_Q$. Here, we have diagonalized the 4×4 real symmetric coefficient matrix, obtaining the eigenvalues $\varepsilon_0 = \varepsilon_1 = 2(J_Q - \lambda)$, $\varepsilon_2 = \varepsilon_+$, and $\varepsilon_3 = \varepsilon_-$ with

$$\varepsilon_\pm = \frac{\omega_0 + \omega_Q + 2\Delta_Q \pm \sqrt{12\Delta_{0Q}^2 + (\omega_0 - \omega_Q - 2\Delta_Q)^2}}{2}. \tag{26}$$

$\{\mathbf{A}_\mu\} \rightarrow \{\Phi_\kappa\}$ is the associated orthogonal transformation

$$\begin{pmatrix} \Phi_0 \\ \Phi_1 \\ \Phi_2 \\ \Phi_3 \end{pmatrix} = \begin{pmatrix} 0 & \frac{2}{\sqrt{6}} & -\frac{1}{\sqrt{6}} & -\frac{1}{\sqrt{6}} \\ 0 & 0 & \frac{1}{\sqrt{2}} & -\frac{1}{\sqrt{2}} \\ \frac{c_+}{\sqrt{c_+^2+3}} & \frac{1}{\sqrt{c_+^2+3}} & \frac{1}{\sqrt{c_+^2+3}} & \frac{1}{\sqrt{c_+^2+3}} \\ \frac{c_-}{\sqrt{c_-^2+3}} & \frac{1}{\sqrt{c_-^2+3}} & \frac{1}{\sqrt{c_-^2+3}} & \frac{1}{\sqrt{c_-^2+3}} \end{pmatrix} \begin{pmatrix} \mathbf{A}_0 \\ \mathbf{A}_1 \\ \mathbf{A}_2 \\ \mathbf{A}_3 \end{pmatrix}, \quad (27)$$

with

$$c_\pm = \frac{\varepsilon_\pm - \omega_Q - 2\Delta_Q}{\Delta_{0Q}}. \quad (28)$$

By adding the Zeeman contribution, we have

$$\begin{aligned} E_{\text{var}} = & \sum_{0 \leqslant \kappa \leqslant 3} \varepsilon_\kappa |\Phi_\kappa|^2 + 2(J_Q - \lambda) \sum_{1 \leqslant \mu \leqslant 3} |\mathbf{B}_\mu|^2 \\ & - \frac{(1-\rho_{\text{imp}})c_+ - 6\rho_{\text{imp}}}{\sqrt{c_+^2 + 3}} H \Phi_2^z \\ & - \frac{(1-\rho_{\text{imp}})c_- - 6\rho_{\text{imp}}}{\sqrt{c_-^2 + 3}} H \Phi_3^z. \end{aligned} \quad (29)$$

From Eq. (29), the magnetic field is expected to induce a collinear triple-Q state because of the magnetic-field coupling to the triple-Q modes $\Phi_{2,3}^z$ [see Eq. (27)] within the Luttinger-Tisza approximation. In fact, by taking derivatives of E_{var} with respect to $\Phi_\kappa^{x,y,z}$ and $B_\mu^{x,y,z}$, we find that a collinear triple-Q state is stable above a threshold magnetic field $H_s \sim 3.39$, whereas it is replaced with a single-Q or other multiple-Q states with different amplitudes for $\mathbf{Q}_1$, $\mathbf{Q}_2$, and $\mathbf{Q}_3$ below H_s. This behavior is at least qualitatively consistent with that observed in our Monte Carlo simulations. However, the resulting triple-Q state is collinear, implying a rather strong violation of the fixed-length constraint. Although, strictly speaking, the violation of the constraint means a breakdown of the Luttinger-Tisza approach, the important implication in this analysis is that mixing of different Q components is indeed expected as a result of the combination of the magnetic field and the special periodic impurities commensurate to modulation of spin texture. In other words, the Luttinger-Tisza approximation provides a simple understanding of the stabilization mechanism of a triple-Q solution, although a more sophisticated variational approach is necessary in order to determine the magnetic structure, as given in the following section.

C. Real-space variational analysis

The above Luttinger-Tisza analysis suggests that a more strict treatment of the constraint is crucial, and the corresponding nonlinear effect is expected to drive the collinear triple-Q state into a noncoplanar multiple-Q state. To proceed, we note that the commensurate Q vectors allow to work on a real-space variational calculation based on the following simple ansatz:

$$S_j = \frac{1}{N_j}\left[\mathbf{M}_0 + \sum_{1 \leqslant \mu \leqslant 3}(\mathbf{M}_\mu e^{i\mathbf{Q}_\mu \cdot \mathbf{r}_j} + \text{c.c.}) \right], \quad (30)$$
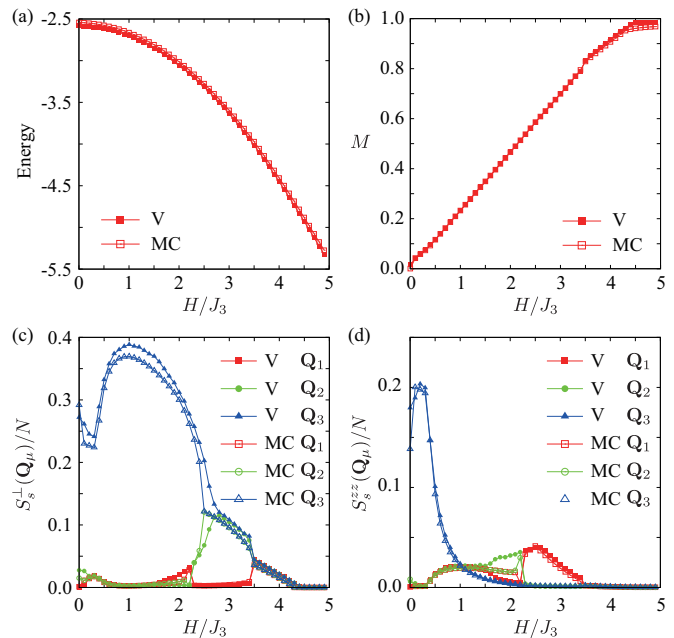

FIG. 7. H dependencies of (a) the energy per site, (b) magnetization, M, (c) $S_s^\perp(\mathbf{Q}_\nu)/N$, and (d) $S_s^{zz}(\mathbf{Q}_\nu)/N$ ($\nu = 1$–3) for $Q = 2\pi/4$ and $a_{\text{imp}} = 8$. "V" and "MC" represent the results obtained by $T = 0$ variational calculations and Monte Carlo simulations at $T/J_3 = 0.05$.

where N_j is a normalization factor which enforces the $S \cdot S = 1$ constraint exactly and $\mathbf{M}_\mu = \mathbf{M}_{-\mu}^*$. The variational parameters are seven: M_0 and three pairs of $(\text{Re}\mathbf{M}_\mu, \text{Im}\mathbf{M}_\mu)$ ($\mu = 1$–3).

Figure 7 shows the H dependence of (a) the energy density, (b) magnetization, (c) the xy component of the spin structure factor, and (d) the z component of the spin structure factor, which are obtained by variational calculations at $T/J_3 = 0.00$ and Monte Carlo simulations at $T/J_3 = 0.05$. The Monte Carlo calculations are consistent with the variational results except for the region $1.6 \lesssim H/J_3 \lesssim 2.1$. The slight deviation around this region is due to a finite-temperature effect in the Monte Carlo simulations. In fact, another phase transition occurs at $T/J_3 \sim 0.03$ for $H/J_3 = 2.0$. Thus, most of the low-temperature phases obtained from the finite-temperature Monte Carlo simulations shown in Fig. 2(a) remain stable down to $T = 0$.

V. TOWARDS MORE REALISTIC CONSIDERATIONS

So far, we have assumed a periodic array of impurities, which is commensurate with the spin texture. Below, we discuss the stability of the chiral phases upon relaxing this condition.

A. Different impurity concentrations

First, we investigate the stability of the chiral phases shown in Fig. 2 upon changing the impurity concentration. Our numerical results and the stability analysis have shown that the multiple-Q structures arise from the fact that $\mathbf{Q}_\nu$ and $\mathbf{Q}_{\nu'}$ ($\nu \neq \nu'$) are connected by $\mathbf{K}_\pm$. Below, we demonstrate that the multiple-Q structure is suppressed upon changing
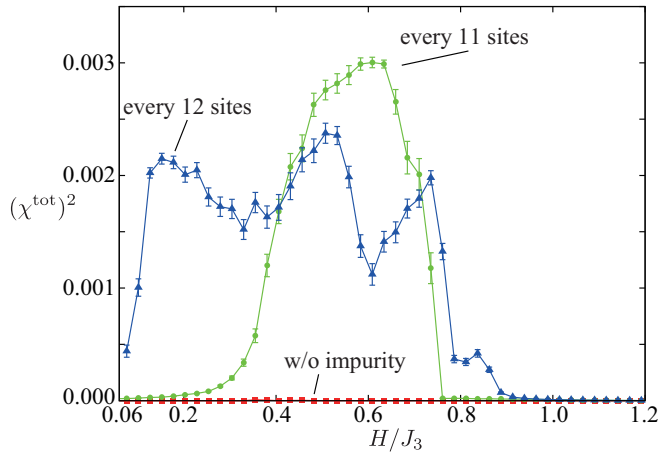
FIG. 8. H dependence of $(\chi^{\text{tot}})^2$ for $J_3/|J_1| \approx 0.394$ ($Q = 2\pi/6$) at $T/J_3 \approx 0.1268$ in the model with or without periodic impurities: $a_{\text{imp}} = \infty$ (no impurities), 12, and 11.

FIG. 10. Allowed positions of a nonmagnetic impurity. Partial randomness is included by locating the nonmagnetic impurities either at a regular superlattice site (the open circle at the origin) or at one of its neighbors (see the text). The filled circles, triangles, and squares denote the NN, second-NN, and the third-NN sites, respectively. The average distance between closest impurities is $\overline{a}_{\text{imp}} = 8$.

the periodicity of impurity array, i.e., upon reducing the commensurability effect.

Figure 8 shows the H dependence of the square of the scalar chirality at a low enough T for several different impurity concentrations and $J_3/|J_1| \approx 0.394$ (corresponding to $Q = 2\pi/6 < Q_c$). In addition to the case without impurities, we show the results for $a_{\text{imp}} = 11$ and 12. The case with $a_{\text{imp}} = 12$ is similar to the case we discussed in Sec. III A, in the sense that $a_{\text{imp}} = 12$ is twice as large as $2\pi/Q = 6$ and $\mathbf{K}_+ + \mathbf{K}_- = \mathbf{Q}_1$ holds. In fact, the H dependence of $(\chi^{\text{tot}})^2$ is qualitatively very similar to the previous case shown in Fig. 2(e). Strictly speaking, the other case with $a_{\text{imp}} = 11$ is also commensurate with the optimal magnetic order. However, the minimal period of the combined structures is 44 lattice spacings, which is significantly large and thus almost incommensurate. Interestingly enough, we find that the net chirality is finite in the intermediate magnetic field range, although the functional form is rather different. The

spin configuration is triple Q^M with vortices located around each impurity (Fig. 9). The corresponding chirality wave has a multiple-Q^χ ferrichiral structure with slightly different profiles in $S^u_\chi(\mathbf{q})$ and $S^d_\chi(\mathbf{q})$. Our results suggest that chiral states resulting from nonmagnetic impurities are rather robust against changing the impurity concentration when Q is small.

B. Skyrmion crystal induced by small randomness

Finally, we introduce small quenched randomness into the array of impurities. In the example of a CDW, nonmagnetic ions (holes or doubly occupied sites) can be frozen at positions slightly away from the perfect superlattice sites. Thus, it is natural to ask what would be the consequence of such small quenched randomness in terms of the magnetic ordering.
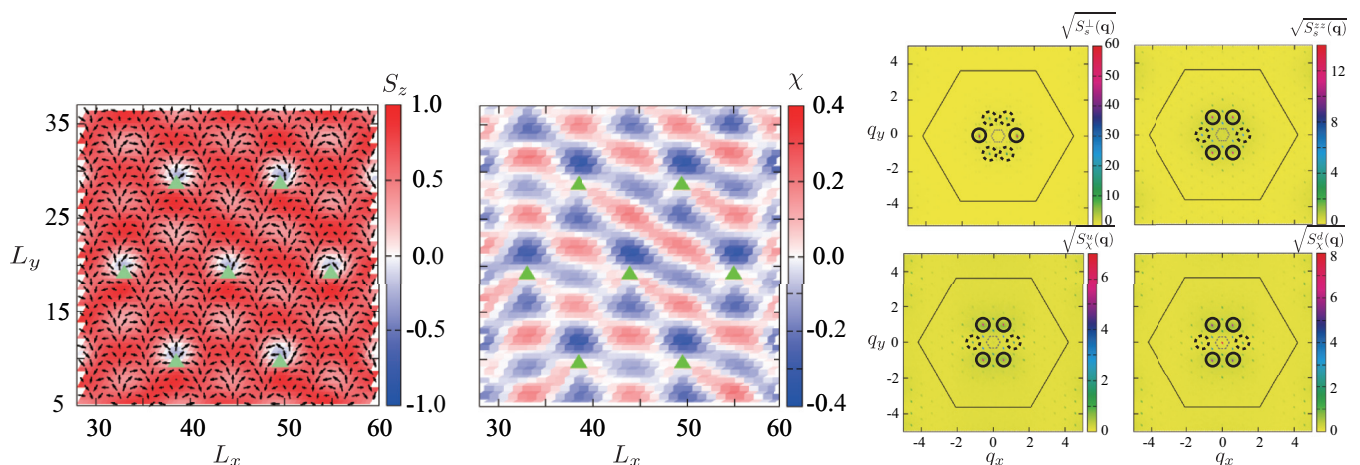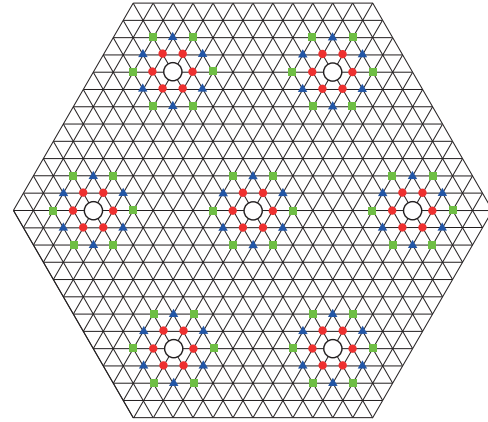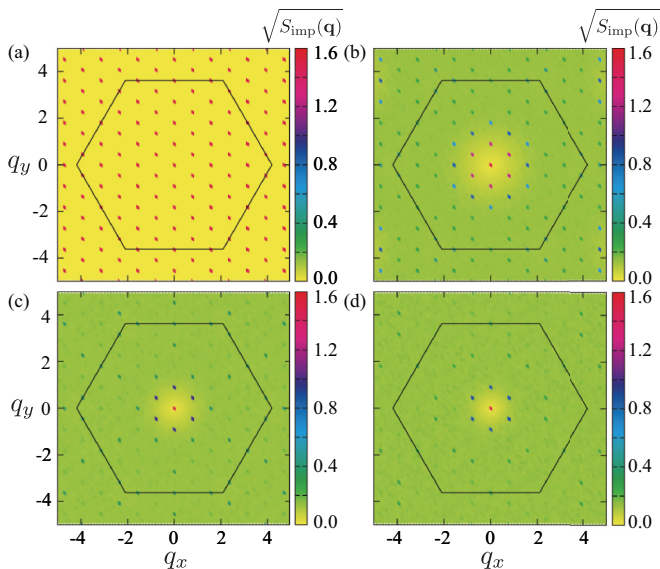

FIG. 9. Snapshots of the spin configuration (left), the chirality texture (middle), and the spin and the chirality structure factors (right) in the model with perfect periodic impurities (triangles) with $a_{\text{imp}} = 11$ for $J_3/|J_1| \approx 0.394$ ($Q = 2\pi/6$) at $H/J_3 \sim 0.634$. The $\mathbf{q} = 0$ component is removed from $S^{zz}_s(\mathbf{q})$. We average over 500 MCS to integrate out short-wavelength fluctuations.

FIG. 11. The impurity structure factors (a) for the regular super-lattice site and with a randomly distribution up to (b) NN sites, (c) second-NN sites, and (d) third-NN sites.

FIG. 13. (a) H dependence of $(\chi^{\text{tot}})^2$ for the model with *partial randomness* of the impurity array $[J_3/|J_1| \approx 0.854 (Q = 2\pi/4)$ and $T/J_3 = 0.05]$. (b), (c) Enlarged views of (a).

To simplify our discussion, we consider the following three cases where, as illustrated in Fig. 10, each nonmagnetic ion is uniformly and randomly placed at (i) one of seven sites comprising a site of the perfect superlattice and its six NNs of the underlying lattice, (ii) one of 13 sites comprising a perfect superlattice site, the six NNs, and the six second NNs or (iii) one of 19 sites that include up to the third-NN sites. For each case, we take statistical averages by generating 32–144 different impurity configurations.

First, we show the impurity structure factor

$$S_{\text{imp}}(\mathbf{q}) = \frac{1}{N} \sum_{j,l} \langle (1 - p_j)(1 - p_l) \rangle e^{i\mathbf{q} \cdot (\mathbf{r}_j - \mathbf{r}_l)}, \qquad (31)$$

for the different randomness (i)–(iii) in Fig. 11. In the case of an ideal impurity array, the Bragg peaks appear at $c_1 \mathbf{K}_+ + c_2 \mathbf{K}_-$ (c_1 and c_2 are integer) with the same intensity, as shown in Fig. 11(a). With increasing the degree of randomness from the case (i) in Fig. 11(b) through the case (iii) in Fig. 11(d), the amplitudes of the Bragg peaks for large $\mathbf{q}$ diminish. In particular, the amplitude at $\mathbf{q} = \mathbf{Q}_\nu$ remains finite (almost disappears) for the cases (i) and (ii) [the case (iii)]. This difference is crucial for the emergence of the skyrmion crystal (see Fig. 12) that we discuss below.

As shown in Figs. 13(a)–13(c), we compute $(\chi^{\text{tot}})^2$ at a low T for $J_3/|J_1| \approx 0.854$ ($Q = 2\pi/4$). While there is no net chirality in the low and high magnetic field regions, we find that the scalar chirality is drastically enhanced in the intermediate field regime $1.2 \lesssim H/J_3 \lesssim 1.6$ for the moderate impurity randomness, i.e., the cases of (i) and (ii), as shown in Fig. 13(c). Such a drastic enhancement indicates the emergence of a new phase induced by the quenched randomness. The spin
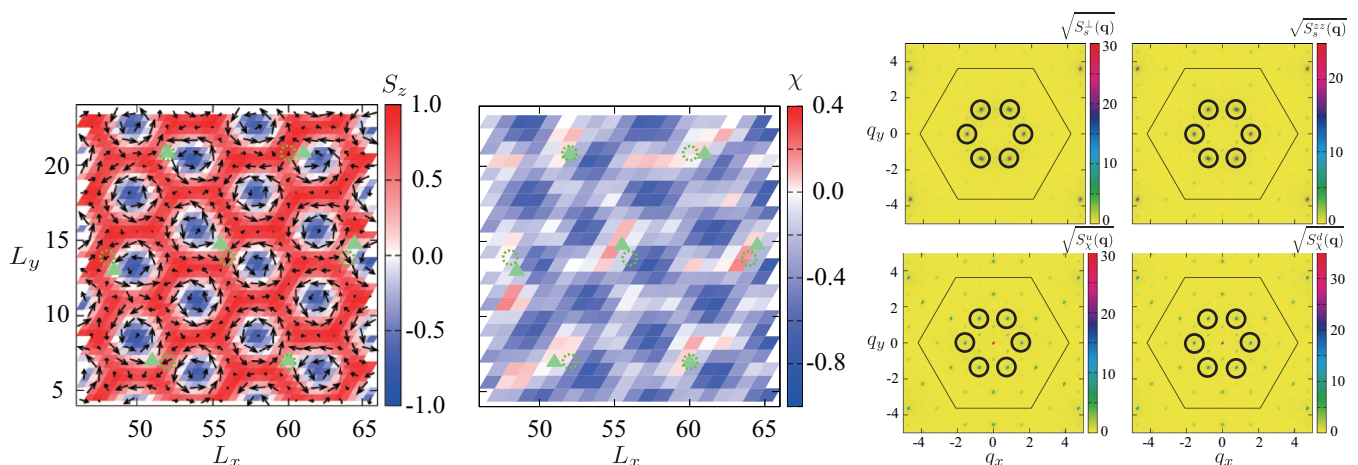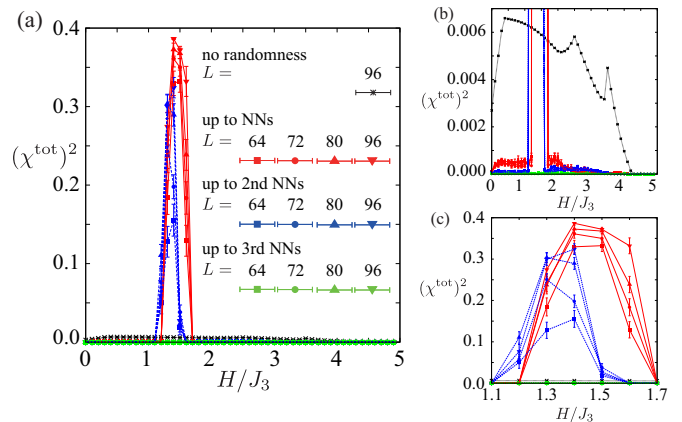

FIG. 12. Snapshots of the spin configuration (left), the chirality texture (middle), and the spin and the chirality structure factors (right) for periodic impurities *slightly disordered up to NNs* (triangles) with $\bar{a}_{\text{imp}} = 8$, $H/J_3 = 1.4$, $T/J_3 = 0.05$, and $J_3/|J_1| \approx 0.854$ ($Q = 2\pi/4$). The dashed circles represent the positions without randomness. The $\mathbf{q} = 0$ component has been removed from $S_s^{zz}(\mathbf{q})$. We average over 500 MCS to integrate out short-wavelength fluctuations.

configuration corresponds to a triple-Q^M hexagonal skyrmion crystal (Fig. 12), similar to the state found by Okubo *et al.* in a different parameter regime of the same model without impurities [21]. A similar phase is also obtained for the same model with easy-axis anisotropy [23–25]. We note that, unlike the ferrochiral $3Q^M$ spiral state in Fig. 4(b), the chirality structure factor of this state shows six peaks at $\mathbf{q} = \pm\mathbf{Q}_{1 \leqslant \nu \leqslant 3}$, in addition to the $\mathbf{q} = \mathbf{0}$ peak (see also Appendix).

The local spin reorientation induced by impurities is central to explain why the skyrmion crystal appears only for small charge randomness in the range of $1.2 \lesssim H/J_3 \lesssim 1.6$. Without the randomness, the ferrochiral $3Q^M$-$2Q^\chi$ spiral I phase is realized in this region, where the spin texture creates the vortex configuration with $S^z \approx 0$ around each impurity. This state is more stable than the skyrmion crystal in the absence of randomness because impurities would be near the center of the skyrmions (commensurability effect). Such a situation is energetically unfavorable due to the large-$|S^z|$ value of the spins near the skyrmion core. (According to our preliminary considerations, the energy is minimized by increasing the xy components of the spins near the nonmagnetic impurities relatively to the other spins.) By introducing the small quenched randomness, as shown in the left panel of Fig. 12, the impurities can escape from the skyrmion core towards the perimeter region where $S^z \approx 0$ and nucleate antivortices around themselves. While the chirality structure is to a large extent characterized by the $\mathbf{q} = \mathbf{0}$ component, as shown in the middle panel in Fig. 12, there are spots with the opposite sign around the impurities because of the induced antivortices. In contrast, the randomness increases the energy of the ferrichiral $3Q^M$-$2Q^\chi$ spiral I phase because it pushes the impurities away from their "comfortable" $S^z \approx 0$ zone. This is also the reason why the skyrmion phase is destabilized when the randomness becomes too strong, i.e., in the case (iii) (see Fig. 13). Once the typical deviation exceeds the skyrmion radius, the impurities are pushed into the large-$|S^z|$ region again. This result points to a new mechanism of stabilizing skyrmion crystals, namely, moderate randomness in the array of nonmagnetic impurities can induce a chiral phase when combined with frustrated exchange interactions.

VI. SUMMARY AND DISCUSSION

As we discussed above, CDW ordering of a strongly coupled single-band model away from half-filling can provide a natural realization of our periodic array of nonmagnetic impurities. Moreover, it is natural to expect that charge orderings which are commensurate with the magnetic ordering wave vectors will be naturally selected at the corresponding filling fractions of the Hubbard model. Our previous analysis of the effect of small randomness in the periodic array of impurities suggests the interesting possibility of having skyrmion crystals stabilized by the zero-point fluctuations of the CDW.

What are the alternative realizations of the model studied in this work? Here, we present three additional proposals for realizing periodic arrays of nonmagnetic impurities. The first realization involves surface science technology [49]. For instance, a selective atom substitution based on the scanning

tunneling microscope technique enables manipulation of atoms on the surface of Mott insulators with spiral order, such as $Fe_xNi_{1-x}Br_2$ [50] and $Zn_xNi_{1-x}Br_2$ [51]. The second possibility is through Kondo lattice systems with long-range Coulomb interaction between conduction electrons. Even not taking into account Coulomb interaction explicitly (i.e., in the usual Kondo lattice model) charge ordering can be induced by magnetic ordering [52–56] and produce a periodic potential for the spin degrees of freedom similar to the one induced by the periodic array of nonmagnetic impurities. Coulomb interactions can enhance this tendency producing an even stronger CDW ordering. In a similar manner, the Hubbard-Holstein model [57,58] and the Hubbard (or t-J) model discussed in the Introduction might provide alternative realizations of a periodic array of nonmagnetic impurities by charge ordering. The third proposal is based on selective Kondo screening: some heavy-fermion compounds are known to exhibit partially ordered magnetic states. For instance, the partially disordered compound UNi_4B exhibits a magnetic vortex structure [59–61]. A possible scenario is that the partial disorder is produced by a site-selective formation of Kondo singlet states [62–64]. The site-selective Kondo screening is then an alternative mechanism for producing a nonmagnetic superlattice.

To summarize, by taking the classical J_1-J_3 Heisenberg model on the triangular lattice as an example, we have shown that exotic multiple-Q states can be induced by periodically distributed nonmagnetic impurities. The interplay between the spin configuration and the underlying impurity superlattice renders most of the states chiral (i.e., with net scalar chirality). We have also shown that weak randomness in the impurity positions, relative to the periodic array, induces a skyrmion crystal phase for intermediate magnetic field values. Our results suggest that a variety of magnetically ordered states with nonzero net scalar chirality can be realized by changing the concentration of nonmagnetic impurities, magnetic field, and temperature.

APPENDIX: CHARACTERIZATION OF EACH PHASE

Figures 14, 15, and 16 show the $1/L$ dependence of the xy and z components of the spin structure factor and the chirality structure factor normalized by the system size N. They should scale $S(\mathbf{q}) \sim O(1), L^{2-\eta}$, and N, respectively, when the corresponding mode is disordered, critical, and long-range ordered. Note that the Mermin-Wagner theorem precludes the long-range order in the xy component at finite T.
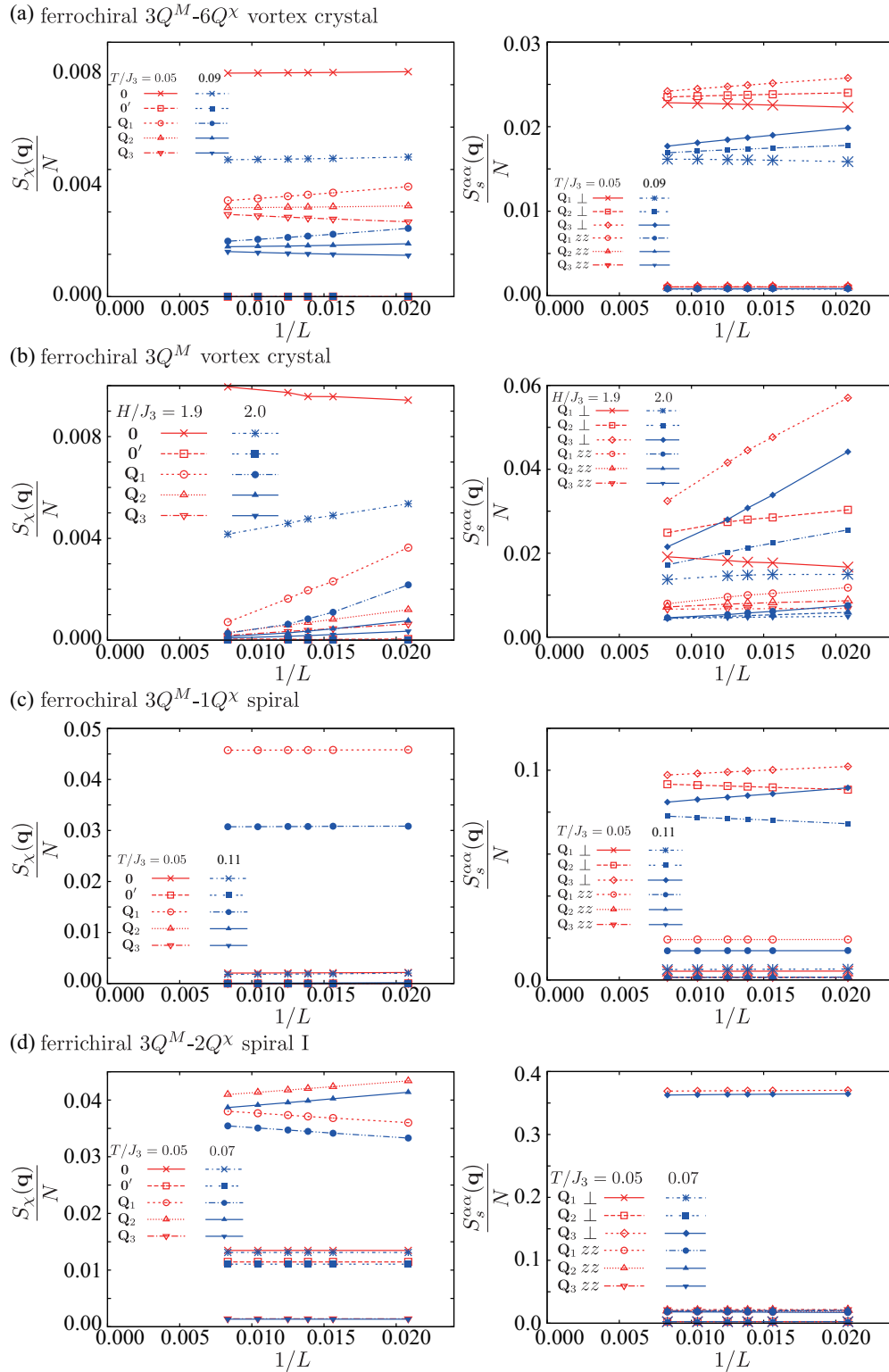
FIG. 14. Size dependence of the order parameters for each phase described in the phase diagram of Fig. 2(c): the chirality structure factor evaluated at $\mathbf{q} = \mathbf{0}, \mathbf{0}', \mathbf{Q}_1, \mathbf{Q}_2, \mathbf{Q}_3$ [$S_\chi(\mathbf{q}) = S_\chi^u(\mathbf{q}) + S_\chi^d(\mathbf{q})$ for $\mathbf{q} = \mathbf{0}, \mathbf{Q}_1, \mathbf{Q}_2$, and $\mathbf{Q}_3$ and $S_\chi(\mathbf{0}') = S_\chi^u(\mathbf{0}) - S_\chi^d(\mathbf{0})$] and the magnetic structure factor at $\mathbf{q} = \mathbf{Q}_1, \mathbf{Q}_2, \mathbf{Q}_3$ in (a) the ferrochiral $3Q^M$-$6Q^\chi$ vortex crystal phase ($H/J_3 = 3.8$), (b) ferrochiral $3Q^M$ vortex crystal phase ($T/J_3 = 0.41$), (c) ferrochiral $3Q^M$-$1Q^\chi$ spiral phase for $Q = 2\pi/4$ ($H/J_3 = 3.0$), and (d) ferrichiral $3Q^M$-$2Q^\chi$ spiral I phase ($H/J_3 = 1.0$) for $Q = 2\pi/4$ and different temperature and magnetic fields.
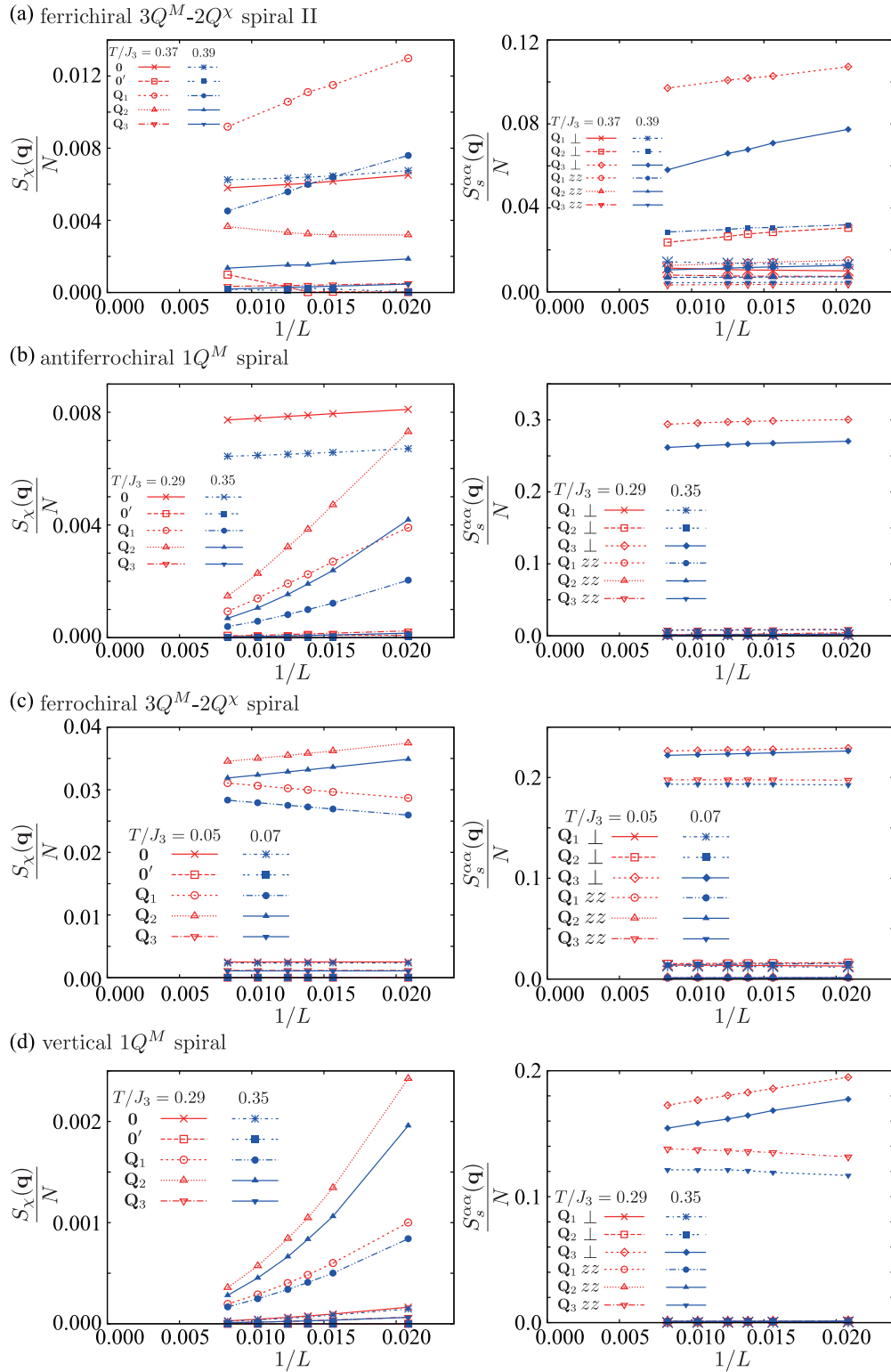
FIG. 15. Size dependence of the order parameters for each phase described in the phase diagram of Fig. 2(c): the chirality structure factor evaluated at $\mathbf{q} = \mathbf{0}, \mathbf{0}', \mathbf{Q}_1, \mathbf{Q}_2, \mathbf{Q}_3$ [$S_\chi(\mathbf{q}) = S_\chi^u(\mathbf{q}) + S_\chi^d(\mathbf{q})$ for $\mathbf{q} = \mathbf{0}, \mathbf{Q}_1, \mathbf{Q}_2$, and $\mathbf{Q}_3$ and $S_\chi(\mathbf{0}') = S_\chi^u(\mathbf{0}) - S_\chi^d(\mathbf{0})$] and the magnetic structure factor at $\mathbf{q} = \mathbf{Q}_1, \mathbf{Q}_2, \mathbf{Q}_3$ in (a) ferrichiral $3Q^M$-$2Q^\chi$ spiral II phase ($H/J_3 = 2.0$), (b) antiferrochiral single-Q^M spiral phase ($H/J_3 = 1.0$), (c) ferrochiral $3Q^M$-$2Q^\chi$ spiral phase ($H/J_3 = 0.2$), and (d) vertical single-Q^M spiral phase ($H/J_3 = 0.2$) for $Q = 2\pi/4$ and different temperature and magnetic fields.
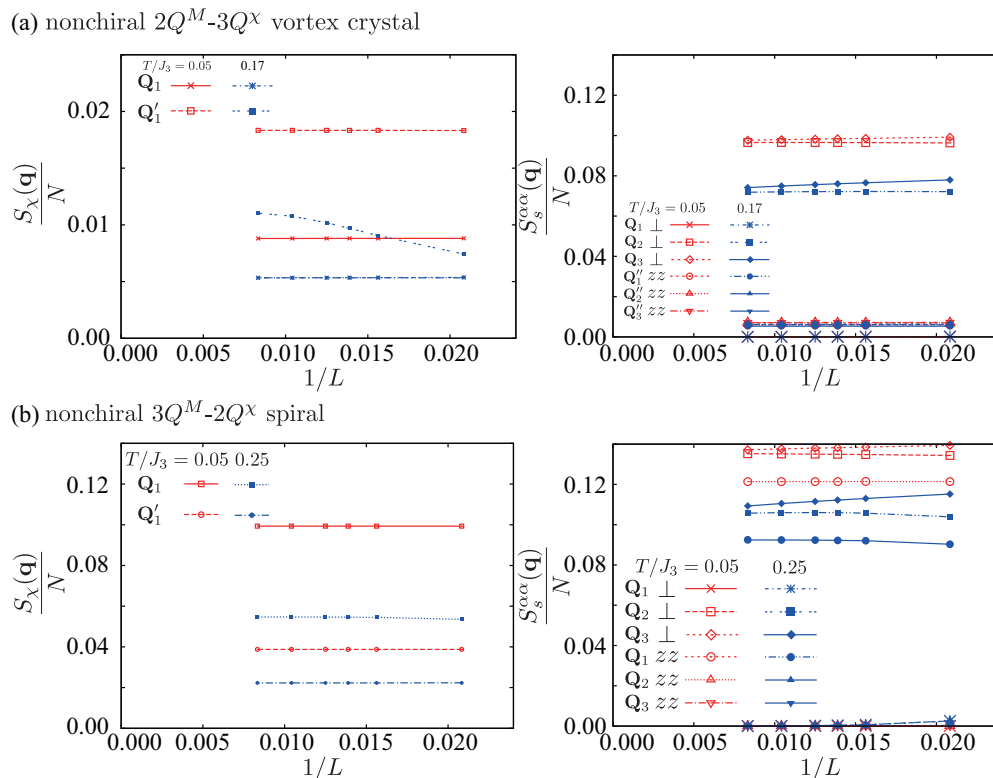
FIG. 16. Size dependence of the order parameters for two phases described in the phase diagram of Fig. 5(b): (a) the xy and z components of the spin structure factor evaluated at $\mathbf{q} = \mathbf{Q}_1, \mathbf{Q}_2, \mathbf{Q}_3$ and the chirality structure factor evaluated at $\mathbf{q} = \mathbf{Q}_1$ and $\mathbf{Q}'_1$ [$Q'_1 = \pi/(2\sqrt{3})$] in the nonchiral $3Q^M$-$2Q^\chi$ spiral phase ($H/J_3 = 1.0$) and (b) the z (xy) component of the spin structure factor evaluated at $\mathbf{q} = \mathbf{Q}''_1, \mathbf{Q}''_2$, and $\mathbf{Q}''_3$ where $Q''_\nu = \pi/\sqrt{3}$ ($\mathbf{q} = \mathbf{Q}_1, \mathbf{Q}_2$, and $\mathbf{Q}_3$) and the chirality structure factor evaluated at $\mathbf{q} = \mathbf{Q}_1$ and $\mathbf{Q}'_1$ in the nonchiral $2Q^M$-$3Q^\chi$ vortex crystal phase ($H/J_3 = 3.0$).

[1] X. G. Wen, F. Wilczek, and A. Zee, Chiral spin states and superconductivity, Phys. Rev. B **39**, 11413 (1989).

[2] H. Kawamura, Chiral Ordering in Heisenberg Spin Glasses in Two and Three Dimensions, Phys. Rev. Lett. **68**, 3785 (1992).

[3] T. Momoi, K. Kubo, and K. Niki, Possible Chiral Phase Transition in Two-Dimensional Solid ^{3}He, Phys. Rev. Lett. **79**, 2081 (1997).

[4] L. N. Bulaevskii, C. D. Batista, M. V. Mostovoy, and D. I. Khomskii, Electronic orbital currents and polarization in Mott insulators, Phys. Rev. B **78**, 024402 (2008).

[5] H. Kawamura, Universality of phase transitions of frustrated antiferromagnets, J. Phys.: Condens. Matter **10**, 4707 (1998).

[6] J.-C. Domenge, P. Sindzingre, C. Lhuillier, and L. Pierre, Twelve sublattice ordered phase in the $J_1 - J_2$ model on the kagomé lattice, Phys. Rev. B **72**, 024433 (2005).

[7] K. A. Al-Hassanieh, C. D. Batista, G. Ortiz, and L. N. Bulaevskii, Field-Induced Orbital Antiferromagnetism in Mott Insulators, Phys. Rev. Lett. **103**, 216402 (2009).

[8] M. V. Berry, Quantal phase factors accompanying adiabatic changes, Proc. R. Soc. London, Ser. A **392**, 45 (1984).

[9] Y. Aharonov and D. Bohm, Significance of electromagnetic potentials in the quantum theory, Phys. Rev. **115**, 485 (1959).

[10] D. Loss and P. M. Goldbart, Persistent currents from Berry's phase in mesoscopic systems, Phys. Rev. B **45**, 13544 (1992).

[11] J. Ye, Y. B. Kim, A. J. Millis, B. I. Shraiman, P. Majumdar, and Z. Tešanović, Berry Phase Theory of the Anomalous Hall Effect: Application to Colossal Magnetoresistance Manganites, Phys. Rev. Lett. **83**, 3737 (1999).

[12] N. Nagaosa, J. Sinova, S. Onoda, A. H. MacDonald, and N. P. Ong, Anomalous Hall effect, Rev. Mod. Phys. **82**, 1539 (2010).

[13] I. Martin and C. D. Batista, Itinerant Electron-Driven Chiral Magnetic Ordering and Spontaneous Quantum Hall Effect in Triangular Lattice Models, Phys. Rev. Lett. **101**, 156402 (2008).

[14] I. Žutić, J. Fabian, and S. Das Sarma, Spintronics: Fundamentals and applications, Rev. Mod. Phys. **76**, 323 (2004).

[15] G.-W. Chern, Noncoplanar Magnetic Ordering Driven by Itinerant Electrons on the Pyrochlore Lattice, Phys. Rev. Lett. **105**, 226403 (2010).

[16] Y. Kato, I. Martin, and C. D. Batista, Stability of the Spontaneous Quantum Hall State in the Triangular Kondo-Lattice Model, Phys. Rev. Lett. **105**, 266405 (2010).

[17] Y. Akagi, M. Udagawa, and Y. Motome, Hidden Multiple-Spin Interactions as an Origin of Spin Scalar Chiral Order in Frustrated Kondo Lattice Models, Phys. Rev. Lett. **108**, 096401 (2012).

[18] S. Hayami and Y. Motome, Multiple-Q instability by (d-2)-dimensional connections of Fermi surfaces, Phys. Rev. B **90**, 060402 (2014).

[19] R. Ozawa, S. Hayami, K. Barros, G.-W. Chern, Y. Motome, and C. D. Batista, Vortex crystals with chirality stripes in itinerant magnets, J. Phys. Soc. Jpn. **85**, 103703 (2016).

[20] S. Hayami, R. Ozawa, and Y. Motome, Engineering chiral density waves and topological band structures by multiple-Q superpositions of collinear up-up-down-down orders, Phys. Rev. B **94**, 024424 (2016).

[21] T. Okubo, S. Chung, and H. Kawamura, Multiple-q States and the Skyrmion Lattice of the Triangular-Lattice Heisenberg Antiferromagnet under Magnetic Fields, Phys. Rev. Lett. **108**, 017206 (2012).

[22] I. Rousochatzakis, U. K. Rössler, J. van den Brink, and M. Daghofer, Kitaev anisotropy induces mesoscopic $\mathbb{Z}_2$ vortex crystals in frustrated hexagonal antiferromagnets, Phys. Rev. B **93**, 104417 (2016).

[23] A. O. Leonov and M. Mostovoy, Multiply periodic states and isolated skyrmions in an anisotropic frustrated magnet, Nat. Commun. **6**, 8275 (2015).

[24] S.-Z. Lin and S. Hayami, Ginzburg-Landau theory for skyrmions in inversion-symmetric magnets with competing interactions, Phys. Rev. B **93**, 064430 (2016).

[25] S. Hayami, S.-Z. Lin, and C. D. Batista, Bubble and skyrmion crystals in frustrated magnets with easy-axis anisotropy, Phys. Rev. B **93**, 184413 (2016).

[26] Y. Kamiya and C. D. Batista, Magnetic Vortex Crystals in Frustrated Mott Insulator, Phys. Rev. X **4**, 011023 (2014).

[27] Z. Wang, Y. Kamiya, A. H. Nevidomskyy, and C. D. Batista, Three-Dimensional Crystallization of Vortex Strings in Frustrated Quantum Magnets, Phys. Rev. Lett. **115**, 107201 (2015).

[28] G. Marmorini and T. Momoi, Magnon condensation with finite degeneracy on the triangular lattice, Phys. Rev. B **89**, 134425 (2014).

[29] B. Binz, A. Vishwanath, and V. Aji, Theory of the Helical Spin Crystal: A Candidate for the Partially Ordered State of MnSi, Phys. Rev. Lett. **96**, 207202 (2006).

[30] B. Binz and A. Vishwanath, Theory of helical spin crystals: Phases, textures, and properties, Phys. Rev. B **74**, 214408 (2006).

[31] J.-H. Park and J. H. Han, Zero-temperature phases for chiral magnets in three dimensions, Phys. Rev. B **83**, 184406 (2011).

[32] Y. Lin, P. Grundy, and E. Giess, Bubble domains in magnetostatically coupled garnet films, Appl. Phys. Lett. **23**, 485 (1973).

[33] A. Malozemoff and J. Slonczewski, *Magnetic Domain Walls in Bubble Materials* (Academic, New York, 1979), p. 382.

[34] N. Kiselev, A. Bogdanov, R. Schäfer, and U. Rößler, Chiral skyrmions in thin magnetic films: New objects for magnetic storage technologies?, J. Phys. D: Appl. Phys. **44**, 392001 (2011).

[35] S. Gao, O. Zaharko, V. Tsurkan, Y. Su, J. S. White, G. S. Tucker, B. Roessli, F. Bourdarot, R. Sibille, D. Chernyshov, T. Fennell, A. Loidl, and C. Rüegg, Spiral spin-liquid and the emergence of a vortex-like state in MnSc$_2$S$_4$, Nat. Phys. (2016), doi:10.1038/nphys3914.

[36] S.-Z. Lin, S. Hayami, and C. D. Batista, Magnetic Vortex Induced by Nonmagnetic Impurity in Frustrated Magnets, Phys. Rev. Lett. **116**, 187202 (2016).

[37] A. Wollny, L. Fritz, and M. Vojta, Fractional Impurity Moments in Two-Dimensional Noncollinear Magnets, Phys. Rev. Lett. **107**, 137204 (2011).

[38] A. Sen, K. Damle, and R. Moessner, Vacancy-induced spin textures and their interactions in a classical spin liquid, Phys. Rev. B **86**, 205134 (2012).

[39] V. S. Maryasin and M. E. Zhitomirsky, Triangular Antiferromagnet with Nonmagnetic Impurities, Phys. Rev. Lett. **111**, 247201 (2013).

[40] V. Maryasin and M. Zhitomirsky, Collective impurity effects in the Heisenberg triangular antiferromagnet, J. Phys.: Conf. Ser. **592**, 012112 (2015).

[41] J. M. Tranquada, D. J. Buttrey, V. Sachan, and J. E. Lorenzo, Simultaneous Ordering of Holes and Spins in La$_2$NiO$_{4.125}$, Phys. Rev. Lett. **73**, 1003 (1994).

[42] J. Tranquada, B. Sternlieb, J. Axe, Y. Nakamura, and S. Uchida, Evidence for stripe correlations of spins and holes in copper oxide superconductors, Nature (London) **375**, 561 (1995).

[43] C. D. Batista, S.-Z. Lin, S. Hayami, and Y. Kamiya, Frustration and chiral orderings in correlated electron systems, Rep. Prog. Phys. **79**, 84504 (2016).

[44] F. R. Brown and T. J. Woch, Overrelaxed Heat-Bath and Metropolis Algorithms for Accelerating Pure Gauge Monte Carlo Calculations, Phys. Rev. Lett. **58**, 2394 (1987).

[45] R. Tamura and N. Kawashima, First-order transition to incommensurate phase with broken lattice rotation symmetry in frustrated heisenberg model, J. Phys. Soc. Jpn. **77**, 103002 (2008).

[46] R. Tamura and N. Kawashima, First-Order Phase Transition with Breaking of Lattice Rotation Symmetry in Continuous-Spin Model on Triangular Lattice, J. Phys. Soc. Jpn. **80**, 074008 (2011).

[47] R. Tamura, S. Tanaka, and N. Kawashima, Phase Transitions with Discrete Symmetry Breaking in Antiferromagnetic Heisenberg Models on a Triangular Lattice, JPS Conf. Proc. **1**, 2125 (2014).

[48] N. D. Mermin and H. Wagner, Absence of Ferromagnetism or Antiferromagnetism in One- or Two-Dimensional Isotropic Heisenberg Models, Phys. Rev. Lett. **17**, 1133 (1966).

[49] D. M. Eigler and E. K. Schweizer, Positioning single atoms with a scanning tunnelling microscope, Nature (London) **344**, 524 (1990).

[50] M. W. Moore and P. Day, Magnetic phase diagrams and helical magnetic phases in M_xNi$_{1-x}$Br$_2$ (M = Fe, Mn): A neutron diffraction and magneto-optical study, J. Solid State Chem. **59**, 23 (1985).

[51] P. Day, M. W. Moore, C. Wilkinson, and K. R. A. Ziebeck, Neutron diffraction study of the incommensurate magnetic phase of Ni$_{0.92}$Zn$_{0.08}$Br$_2$, J. Phys. C: Solid State Phys. **14**, 3423 (1981).

[52] S. Reja, R. Ray, J. van den Brink, and S. Kumar, Coupled spin-charge order in frustrated itinerant triangular magnets, Phys. Rev. B **91**, 140403 (2015).

[53] T. Misawa, J. Yoshitake, and Y. Motome, Charge Order in a Two-Dimensional Kondo Lattice Model, Phys. Rev. Lett. **110**, 246401 (2013).

[54] S. Hayami, T. Misawa, Y. Yamaji, and Y. Motome, Three-dimensional Dirac electrons on a cubic lattice with noncoplanar multiple-Q order, Phys. Rev. B **89**, 085124 (2014).

[55] S. Hayami, T. Misawa, and Y. Motome, Charge Order with a Noncoplanar Triple-Q Magnetic Order on a Cubic Lattice, JPS Conf. Proc. **3**, 016016 (2014).

[56] H. Ishizuka, M. Udagawa, and Y. Motome, Magnetic order and charge disproportionation in a spin-ice type kondo lattice model: Large scale monte carlo study, J. Phys. Soc. Jpn. **81**, 113706 (2012).

[57] S. Kumar and J. van den Brink, Charge ordering and magnetism in quarter-filled Hubbard-Holstein model, Phys. Rev. B **78**, 155123 (2008).

[58] K. Pasrija and S. Kumar, Noncollinear and noncoplanar magnetic order in the extended Hubbard model on anisotropic triangular lattice, Phys. Rev. B **93**, 195110 (2016).

[59] S. A. M. Mentink, A. Drost, G. J. Nieuwenhuys, E. Frikkee, A. A. Menovsky, and J. A. Mydosh, Magnetic Ordering and Frustration in Hexagonal UNi_4B, Phys. Rev. Lett. **73**, 1031 (1994).

[60] A. Oyamada, M. Kondo, K. Fukuoka, T. Itou, S. Maegawa, D. X. Li, and Y. Haga, NMR studies of the partially disordered state in a triangular antiferromagnet UNi_4B, J. Phys.: Condens. Matter **19**, 145246 (2007).

[61] S. Hayami, H. Kusunose, and Y. Motome, Toroidal order in a partially disordered state on a layered triangular lattice: implication to UNi_4B, J. Phys.: Conf. Ser. **592**, 012101 (2015).

[62] C. Lacroix, B. Canals, and M. D. Núñez-Regueiro, Kondo Screening and Magnetic Ordering in Frustrated UNi_4B, Phys. Rev. Lett. **77**, 5126 (1996).

[63] Y. Motome, K. Nakamikawa, Y. Yamaji, and M. Udagawa, Partial Kondo Screening in Frustrated Kondo Lattice Systems, Phys. Rev. Lett. **105**, 036403 (2010).

[64] S. Hayami, M. Udagawa, and Y. Motome, Partial disorder in the periodic anderson model on a triangular lattice, J. Phys. Soc. Jpn. **80**, 073704 (2011).